Czech Technical University in Prague
Faculty of Civil Engineering
Department of Mechanics

Ing. Jiří Němeček, Ph.D.

Nanoindentation of Heterogeneous Structural Materials

Habilitation thesis

Prague, September 2009

Acknowledgements

Contents

List of Figures

List of Tables

9

Abstract

This habilitation thesis aims to apply some well established as well as new approaches to heterogeneous structural materials using powerful micromechanical experimental technique, the nanoindentation. The technique is described in broad details that are highly important for analysis of inhomogeneous solids and special attention is given to evaluation and interpretation of its results for this kind of complex materials. Several approaches are proposed in conjunction with numerical and statistical evaluation, such as statistical grid indentation, deconvolution algorithms or pointed indentation.

Two basic representatives of structural materials, namely cement paste and alkali-activated fly ash (AAFA), are investigated throughout this study, some unique outcomes are summarized and possible interpretations are carefully provided with the results in the work. Intrinsic mechanical properties of cement paste and AAFA were identified by means of statistical nanoindentation. Some material phases, such as clinkers, or high-density C-S-H, were measured by direct method, i.e. pointed indentation. Results were examined together with the knowledge of chemistry and other supplementary measurements like porosimetry, ESEM and EDX analyses. Results were in good agreement with those found in the literature in case of cement paste while in case of AAFA the measurement provided a pioneer work in this field. Up-scaling of intrinsic elastic micromechanical properties to meso-level was also demonstrated for cementitious composite using simple analytical homogenization tools.

Inelastic properties were analyzed for the case of cementitious samples and estimation of their viscoelastic properties is provided in this work based on analytical solution of a four parameter combined Kelvin-Voigt-Maxwell chain.

Numerical modeling of nanoindentation process was studied in the last chapter of this thesis. A general finite element model was constructed and the comparison of several constitutive models was shown. Based on experimental results from cyclic tests it was concluded that simple viscoelastic solution can capture the loading and holding periods of the P-h curve for one

cycle experiment. However does not lead to satisfactory results for the case of cyclic loading. The FE analyses showed that in description of the micromechanical behavior of cement paste, both time-independent plastic strains and time-dependent creep stains appear to play an important role. The model that combined nonlinear viscoelastic and plastic elements provided the best qualitative match to the experimentally measured response also for complex loading histories like cyclic loading.

Nanoindentation was found to play an indispensable role in identifying of phase properties of heterogeneous materials and its application to structural ones open a path to wide variety of interesting research topics that can be hardly solved by using of some other mechanical tests.

Notation

Material properties and nanoindentation

P ... loading force
h ... penetration depth
E_r ... reduced modulus
E ... Young's modulus
H ... hardness
ν ... Poisson's ratio
k ... bulk modulus
μ ... shear modulus

Tensor notation

$\mathbf{u}$ ... first-order tensor, e.g. displacement tensor
$\boldsymbol{\varepsilon}$ ... second-order tensor, e.g. strain tensor
$\mathbf{C}$ ... fourth-order tensor, e.g. stiffness tensor

Cement and aluminosilicate terminology

C-S-H ... calcium-silica-hydrate
CH ... calcium hydroxide, Portlandite
C_3S ... tricalcium silicate
C_2S ... dicalcium silicate
C_3A ... tricalcium aluminate
C_4AF ... tetracalcium aluminoferrite
w/c ... water-to-cement mass ratio
ITZ ... interfacial transition zone
N-A-S-H ... aluminosilicate gel
AAFA ... alkali-activated fly ash
AAMK ... alkali-activated metakaolin

Other abbreviations

AFM ... atomic force miscroscope
ESEM ... environmental scanning electron microscope
BSE ... back-scattered electrons
MIP ... mercury intrusion porosimetry

Chapter 1

State-of-the-art

1.1 Introduction

Nanoindentation is a powerful experimental technique which is being developed for more than a decade together with precise device fabrication, characterization of lower scale physical laws, theories and small scale numerical modeling. Nowadays, it is fairly widely used for assessing of mechanical properties of small material volumes at nano and micrometer range.

The principle of nanoindentation lies in bringing a very small tip to the material surface producing an imprint. It is used for obtaining material parameters like elastic modulus, hardness, plastic or viscous parameters from experimental readings of indenter load and depth of penetration. Forces involved are usually in the mili or micronewton range and the depth in the order of nanometers. Different kinds of probes can be used for making an imprint into the material surface [2].

The main advantage compared to classical mechanical tests is that a very small material volumes having typically the order of several tens of nanometers can be accessed with the tip of the nanoindenter and material properties can be evaluated for such a small piece of the material. When testing such small volumes one should realize which material or structural feature can be affected. For illustration, some typical ones are summarized in Tab. 1.1.

1.2 Heterogeneity and multiscale materials

Standardly, some fine materials are considered, measured and also modeled as homogeneous. But their homogeneity must be viewed from the perspective of different length scales. For example, if we consider the whole structure of a building, the material like steel or concrete can be considered as homogeneous

Table 1.1: Length scales of some typical features.

Feature	Typical dimension
Concrete aggregate	$10 - 100$ mm
Sand particle	$0.1 - 1$ mm
Human hair	$50 - 100$ μm
Cement clinker grain	$10 - 100$ μm
Gel structures in hydrated cement	$\approx 10 - 100$ nm
C-S-H gel globules [3]	≈ 5 nm
Carbon nanotubes SWNT	≈ 2 nm
Water molecule	3.1 nm
Atom of carbon	0.1 nm

without any problems. But if we downscale our view to a structural element we can see joints, layers, material inhomogeneity etc.

In case of analyzing the material the situation is very much the same. Strictly speaking, every material is heterogeneous at certain length scale. In case of a structural material like concrete it is usually treated as so called multiscale material in which we can distinguish some typical length scale levels (e.g. [4, 5, 6, 7]). On these separate levels the material is considered as homogeneous. So we split the material to levels (e.g. Fig. 1.1) that are assumed to be homogeneous or the homogeneous properties are computed from intrinsic properties of their components using some homogenization technique to obtain its effective overall property (see [8] for review).

100 nm   10 μm   1 mm   10 mm
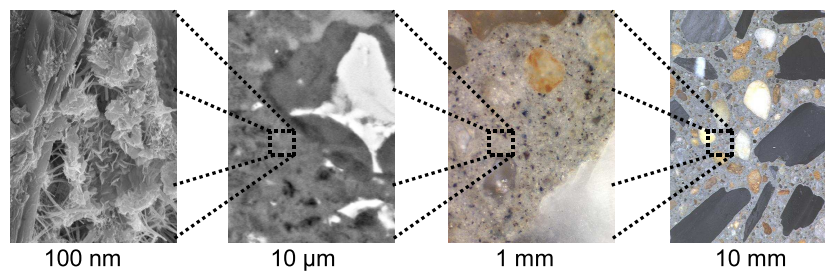
Figure 1.1: Concrete viewed as a multiscale material.

1.3   Principle of nanoindentation

Nowadays, nanoindentation is probably the only experimental technique that can be used for direct accessing mechanical properties at material microlevel. It is based on the measurement of the load versus penetration relationship using a very small (usually diamond) tip pressed into a material (Fig. 1.2). With this method, it is possible to assess bulk elastic properties, such as Young's modulus, hardness and viscosity of material volumes with dimensions on the nanometer scale. Therefore, nanoindentation offers results in the point-wise estimates of locally homogenized data (in nm scale). Nanoindentation has been widely used for metals, glass or ceramics. However, its use for heterogeneous and porous materials such as cementitious composites, where it could disclose micromechanical properties of individual cement components, interfacial zones, fibers, aggregate, etc., is rare. For instance, Velez et al. [9], determined intrinsic properties of individual cement clinkers, Constantinides and Ulm [10] investigated elastic properties of two types of C-S-H gels in cement paste and their chemical degradation.
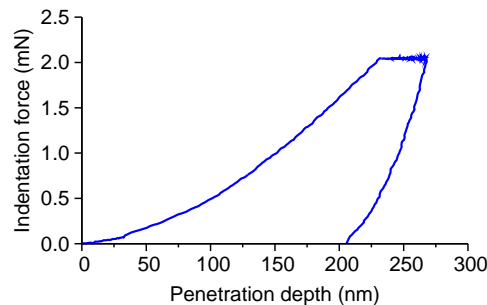
Figure 1.2: Typical load versus penetration diagram from nanoindentation.

As already mentioned, the principle of nanoindentation lies in bringing a very small tip to the material surface producing an imprint (Fig. 1.3). Two basic parameters are monitored in the apparatus: force and displacement (i.e. penetration depth). In the simplest case, the test includes loading and unloading as shown in Fig. 1.4. From nanoindenter, just one axial deflection in the vertical axis can be utilized. So, the surrounding surface deflections must be deduced by other means (by independent measurements or modeling). Residual imprints can be visualized, for example, by atomic force microscope (AFM, Fig. 1.5).

The loading diagram can be modified for different solids. Elasto-plastic materials do not exhibit time-dependent behavior and thus loading/unloading can be sufficient for describing their behavior while time-dependent materials

exhibit also viscous flow during loading process and thus additional segments such as holding periods are often included in the loading diagram (Fig. 1.6) to measure creep, for instance.
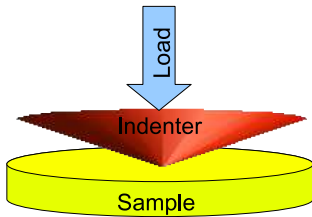
Figure 1.3: Principle of nanoindentation.
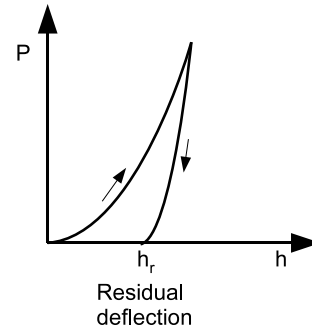
Figure 1.4: Loading diagram.
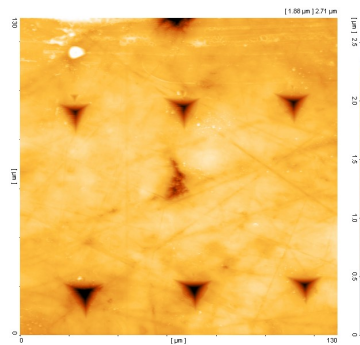
Figure 1.5: AFM image of imprints in cement paste after nanoindentation.

1.4 Instrumentation

Nowadays, nanoindenters are produced by several international companies. They are using slightly different principles and they also differ in certain abilities. The major nanoindenter producers are:

- Hysitron Inc., USA

- Micromaterials Ltd., UK

- CSM, Switzerland
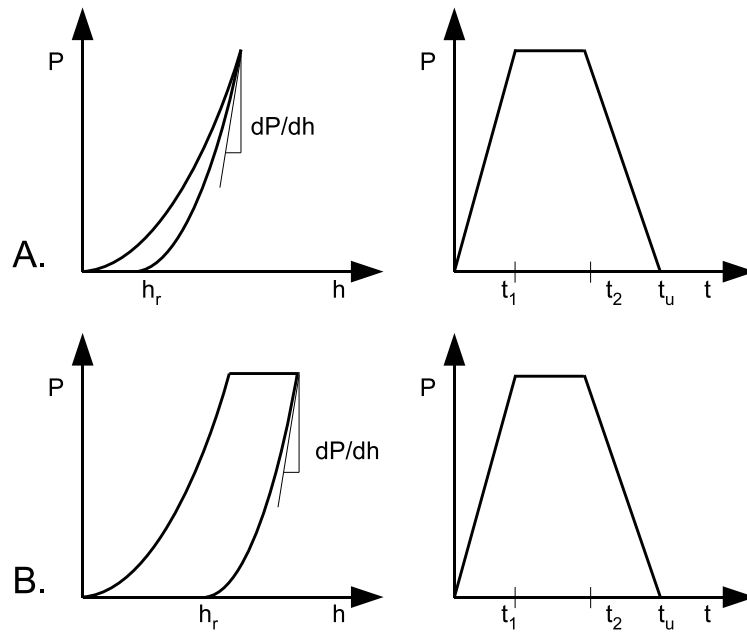
Figure 1.6: A. Load-depth and load-time plots for elastic-plastic solid, B. Load-depth and load-time plots for visco-elasto-plastic solid.

• MTS Systems Corporation, USA

Results further used in this work were obtained by using mainly the first three machines so they will be discribed in some details here.

Besides standard quasi-static testing, Hysitron Tribolab system (Fig. 1.7) is capable of in-situ SPM imaging in which the same tip is used for scanning of the sample as for indentation as in case of AFM (Fig. 1.8). It is equipped with nanoDMA module for dynamic testing in the range 0 – 300 Hz. It can be used for modulus mapping and scratch test. The loading range is 100nN – 30mN (@3nN) and the Z-resolution is 0.2 nm. Both load and depth control regimes are applicable. Due to low forces applied it is necessary to use an active anti-vibration table. The apparatus is placed in a closed chamber in order to achieve thermal stability.

In contrast to Hysitron, Nanotest by Micromaterials (Fig. 1.9) uses a pendulum system in which the indentation axis is put to horizontal position (Fig. 1.10). Simple temperature and humidity chamber is provided with the machine. Zoom optical microscope (magnification up to 40×) is installed. High load 0.1 – 20 N and low load head 0.1 – 500 mN are available for testing. As an additional feature, the high temperature stage up to 500°C can be used.

Figure 1.7: Hysitron Tribolab system.
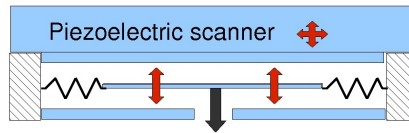
Figure 1.8: Scheme of Hysitron 2D transducer used for in-situ SPM imaging.

Probably one of the most robust nanoindentation systems is produced by CSM Instruments. In our laboratory, it is installed inside a high-end climatic chamber (Fig. 1.11), it has high resolution optical microscopes ($5\times$ and $100\times$) that can produce, together with CCD camera, almost $4000 \times$ magnification. The load range lies in between $0.1 - 500$ mN and the depth resolution is 0.5 nm. CSM uses the reference-ring system for easy and fast surface detection. It can be used for static and dynamic testing (the sinus mode is limited to $0 - 20$ Hz).

Figure 1.9: Nanotest, Micromaterials, UK.
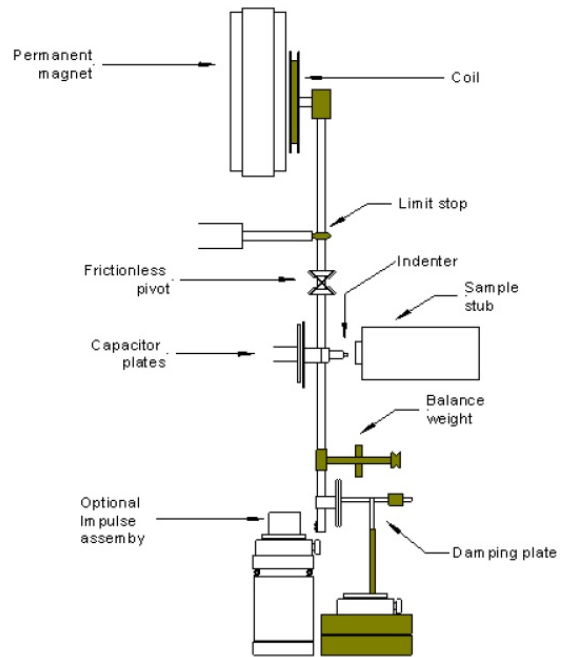
Figure 1.10: Pendulum system of Nanotest.

Figure 1.11: CSM Nanohardness tester.

1.5 Standard evaluation of experimental results for homogeneous bodies

Standardly, the elastic and inelastic materials' constants are derived from nanoindentation test data using analytical solutions typically applicable to homogeneous and isotropic half-space with a flat surface. The limitations of such solutions are further corrected by calibrations and semi-analytical factors for real geometries of a punch.

An elastic contact problem was solved already in the far history by Hertz [11] in 1881 when he found solution of elastic contact of two spheres with different radii. In 1885, Boussinesq [12] solved stresses and displacements in an elastic body loaded by a rigid axisymmetric indenter. In 1965, Sneddon [13] formulated a general relationship between load, displacement and contact area for any punch described as a solid of revolution of a smooth function. The Sneddon's load-displacement relationship for an elastic solid can be expressed by general equation as:

$$P = \alpha h^m \tag{1.1}$$

where P is the load, h is the displacement, α and m are constants ($m = 1$ for a flat cylinder, 2 for cone, 1.5 for spheres).

If we analyze the loading diagram of the real material that is usually not only elastic we can apply this solution to the unloading part which, in many cases, can be successfully supposed to be elastic (Fig. 1.12). The situation under the indenter at maximum deflection and after unloading is described in Fig. 1.13. For a cone, the Sneddon's solution gives:

$$P = \frac{\pi a}{2} E_r a cot\alpha \tag{1.2}$$

where E_r is the reduced modulus (which accounts for non-rigid indenter) and the surface deflection is given by

$$h = \left(\frac{\pi}{2} - \frac{r}{a}\right) a cot\alpha, \quad \text{for} \quad r \leq a. \tag{1.3}$$

Two elastic constants are usually derived from experimental data: hardness and elastic modulus. Hardness is defined as the mean contact pressure at the maximum load:

$$H = \frac{P_{max}}{A} \tag{1.4}$$

in which A is the projected contact area of the indenter at the peak.

To evaluate elastic constants, maximum force, deflection and tangent at the peak (P_{max}, h_{max} and $\frac{dP}{dh}|_{P_{max}}$) can be read from experiments (see Figs 1.12

and 1.13). Combining Eq. (1.2) with Eq. (1.3) one can derive reduced modulus as:

$$E_r = \frac{dP}{dh} \frac{1}{2} \frac{\sqrt{\pi}}{\sqrt{A}}. \tag{1.5}$$

And using contact mechanics (Hertz's solution of two non-rigid bodies) an elastic modulus E can be assessed as:

$$\frac{1}{E_r} = \frac{(1 - \nu^2)}{E} + \frac{(1 - \nu_i^2)}{E_i} \tag{1.6}$$

in which E_r is the reduced modulus (or combined modulus) measured in an experiment, ν is Poisson's ratio of the material, E_i and ν_i are elastic modulus and Poisson's ratio of the indenter, respectively.
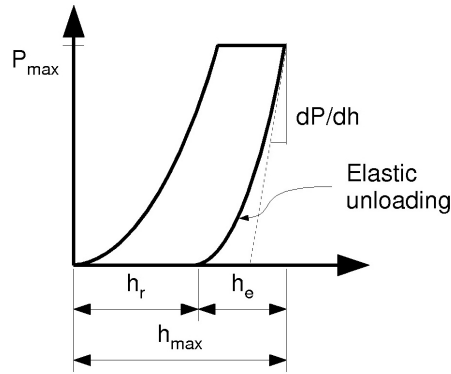
Figure 1.12: Loading diagram.
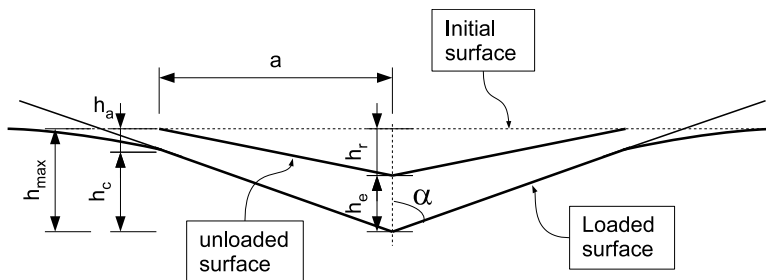
Figure 1.13: Situation under the indenter.

The non-conical indenters are usually treated with an equivalent cone angle α. For example, the three-sided pyramidal tip, Berkovich, has $\alpha =$

70.3^o. The problem with analyzing of experimental data is in the description of the unloading branch and contact area under the indenter. Probably the most popular evaluation methodology was elaborated by Oliver and Pharr [14] in which the contact depth is given by

$$h_c = h_{max} - \varepsilon \frac{P_{max}}{\frac{dP}{dh}}. \qquad (1.7)$$

Factor ε depends upon geometrical shape of an indenter (Tab. 1.2). Hardness can be computed according to Eq. (1.4) and the reduced modulus as:

$$E_r = \frac{dP}{dh} \frac{1}{2\beta} \frac{\sqrt{\pi}}{\sqrt{A}}. \qquad (1.8)$$

Geometrical factor β (see Tab. 1.3) has been introduced to correct non-symmetrical indenter shape compared to cone and it was assessed by FE calculations (King [15]).

Table 1.2: Indenter shape factor.

Indenter shape	ε
conical	0.7268
flat punch	1
paraboloid of revolution, Berkovich	0.75

Table 1.3: Geometrical factor β.

Shape	ε
circular	1.0
triangular (Berkovich)	1.034
square	1.012

Chapter 2

Nanoindentation of heterogeneous materials

2.1 Heterogeneity of structural materials

Structural materials exhibit several types of heterogeneity at microscale. The first type of heterogeneity comes from mixing of components that do not chemically react in the matrix like sand, fibers, and other additives. Such heterogeneity is usually known in advance and is given by the mixing proportions. The second type of heterogeneity comes from chemical reactions that are evolving after the mixing of components. As a result of these reactions, new phases are produced and it is hard to rigorously define their volumes and distribution. Formation of the new phases includes fully reacted matrix, unreacted grains of the raw material and interfacial zones with different chemical and also mechanical properties (e.g. [16, 17, 18, 19]) and porosity. Structural materials based on cement (like cement paste, concrete) or waste materials (like fly-ash, furnace slag, etc.) usually include both types of the heterogeneity. An example of two structural materials is shown in Figs 2.1 and 2.2. It can be seen from these ESEM images that we are facing high degree of heterogeneity at and even below the micrometer range.

   Therefore, micromechanical analysis of any heterogeneous material involves several subsequent steps that cannot be omitted. The first step includes microstructural observations and determination of phases. This step can be performed with the aid of many experimental techniques. Among others, the most common technique is an electron microscopy (ESEM) and atomic force microscopy (AFM). These techniques allow qualitative as well as quantitative investigation of individual material phases at small volumes near or at the sample surface. As a complementary computational technique,
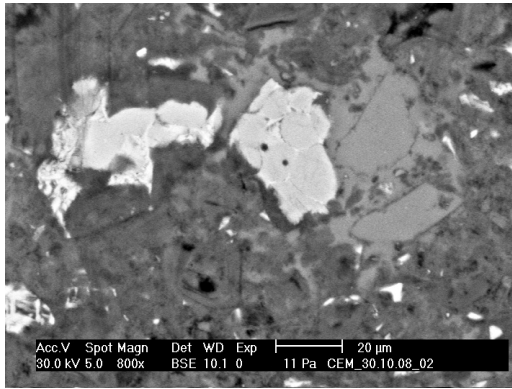
Figure 2.1: ESEM image of hydrated cement paste. Dark areas= pores; dark grey= C-S-H gels; light grey= Portlandite; light areas= unreacted clinker.
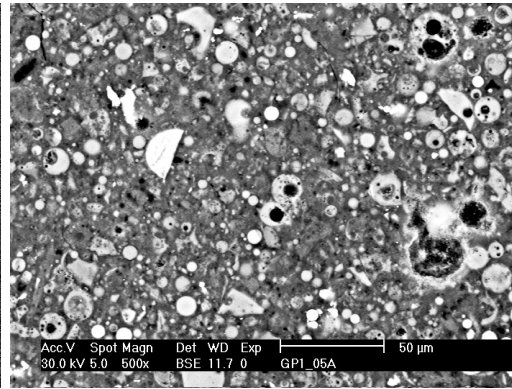
Figure 2.2: ESEM image of alkali-activated fly ash. Light and light grey areas= unreacted or partly reacted fly-ash grains; dark grey areas= polymer zone; dark areas= pores.

image analysis can give valuable results for the phase distribution based on the separation of pixel colors.

The second step includes the measurement of intrinsic properties of individual material phases. It can be provided exclusively by nanoindentation which is the only technique that can directly access mechanical properties at small dimensions starting from several tens of nanometers (depending on the sample and the probe).

The third step involves up-scaling of the properties to the higher level (meso/macrolevel). Several analytical or numerical homogenization techniques can be employed to reach this goal, e.g. [8, 20, 5].

In contrast to usual indentation on homogeneous glass, films, coatings, metals or ceramics, structural materials like cement paste are much more complex. Their heterogeneity is further complicated also by their loading time dependence, aging and property fluctuations due to temperature or humidity [21].

The evaluation methodology however, is currently restricted to homogeneous systems. Direct application of Eqs (1.4) and (1.5) to multiscale materials poses several difficulties, as the underlying analysis relies on the self-similarity of the indentation test which holds only for homogeneous materials [22]. The interaction of phases in multiscale materials is unavoidable but depending on the length scales it can be more or less important as will be discussed in the next section.

2.2 Scale separation

Indentation analysis of homogeneous materials is independent on length scales and so on the indentation depth h [23]. In order to describe heterogeneous systems and their effective properties in a statistical sense, representative volume element (RVE) have been introduced [24, 25]. The transition from a heterogenenous material at a lower level to a homogeneous material at a higher level is ensured by a scale separation inequality:

$$d << L << (h, D) \tag{2.1}$$

where d is the characteristic size of the largest microstructural inhomogeneity, L is the RVE size and D is a characteristic microstructural length scale. If the Eq. (2.1) is satisfied, an indentation experiment performed to an indentation depth h gives access to the material properties that are characteristic of the material at a length scale of L including all underlaying inhomogeneities. In case of a structural material, these inhomogeneitites can be porosity or internal polymeric structures, etc.

As already mentioned, standard nanoindentation data processing (Oliver and Pharr [14]) is based on homogeneous-like solutions with no scale limit, where the self-similarity applies. Therefore, the properties extracted from indentation data of a heterogeneous solid are averaged quantities dependent on the depth h. For example, the effective volume affected by an indent can be estimated as three times of the penetration depth h for the Berkovich indenter [26]. Therefore, the choice of an indentation depth directly determines the length scale of the material RVE.

Composite structural materials are multiphase materials in which distinct phases are intermixed spatially and chemically. Taking the microstructural heterogeneity into account one can formulate basically three testing strategies to obtain mechanical properties of a composite or its phase properties.

1. Averaged (effective) composite properties can be found if the indentation depth is larger than the characteristic phase dimension ($h >> D$). In this case, a phase compound is indented and thus, physically averaged properties are obtained. This strategy does not give access neither to distinct phases' properties nor to their volume fractions.

2. Another possibility is to perform pointed indentation to a specific material phase with indent's dimension smaller then the characteristic dimension of the tested phase ($h << D$). In this case, intrinsic properties of the distinct phase (but including intrinsic phase porosity, for example, which lies below the tested size h) are obtained. This strategy can

be used, provided the material phase can be distinguished prior to indentation by some other means (e.g. optical microscope, ESEM) which is not always the case. It gives access to the distinct phase properties but not to volume fraction of the phase compared to other phases.

3. The last one, but for structural materials probably the most powerful technique, is based on the statistical (massive grid) indentation in which indents are produced over a large area to capture the sample heterogeneity but the dimension of a single indent is still smaller than the characteristic dimension of an individual phase ($h << D$).

   In this case, the results provide information on all phases' properties as well as their volume ratios but without any knowledge which indent belongs to which phase. The properties can be evaluated in terms of property histograms for which subsequent deconvolution techniques can be employed and individual phase properties assessed [22].

All the approaches are schematically shown in Fig. 2.3 for a three phase medium. Different property histograms are received and, as explained, they must be viewed from the perspective of proper scale separation.

However, the methodologies described in items #2 and #3 can provide the access to intrinsic phase properties only in case that the indentation response of one phase is not influenced by another. It means that not only the geometrical factor of indentation depth but also mechanical properties of distinct phases matter. As a rule of a thumb, the indentation depth is usually chosen as 1/10 of the characteristic size D [27, 28]. The situation of phases with different stiffnesses was studied for thin films placed on a substrate (e.g. Gao et al. [29]). It was shown by Gao that the substrate effects are negligible for stiffness mismatch ratio $E_s/E_f \in [0.2, 5]$ as long as the indentation depth h is smaller than 10% of the film thickness. The layered substrate–film system is not completely equivalent to the disordered structural multiphase materials but it can be succesfully used as the first estimate.

In many cases, material phases can hardly be distinguished. For example, C-S-H gels of different densities (low and high) are intermixed with Portlandite zones in hydrated cement matrix. There is no exact means of chemical or optical differentiation between them and therefore pointed indentation (item #2) is not possible in this case. Hence, the assessment of intrinsic phase properties leads to using of approach #3. However, in such a case, properties received from grid indentation have to be deconvoluted into distinct phase distributions.
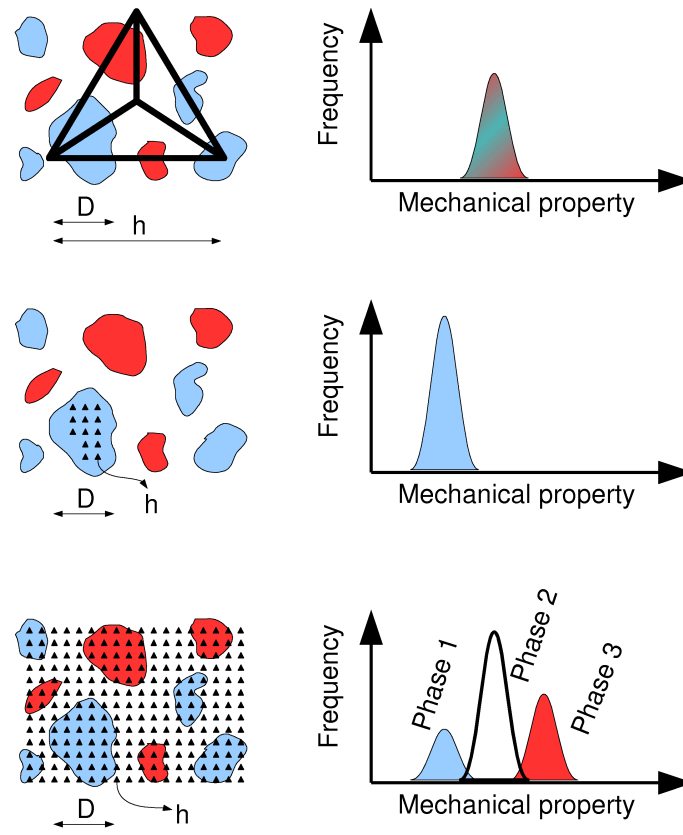
Figure 2.3: Schematic representation of three testing strategies. Top: Large indent producing average properties. Middle: Small indents pointed into one phase. Bottom: Large grid of small indents produced over large sample area. The overall property histogram is a convolution of results from several phases in this case.

2.3 Statistical Deconvolution

For heterogeneous materials, individual phase properties can be determined by the statistical deconvolution applied to histograms of any mechanical property like E modulus, for example. The deconvolution procedure here was adopted from [26] but different minimizing criteria and a different generation of random sets of probability functions were used as will be demonstrated in the following.

Experimental histograms are constructed from all measurements whose number is N^{exp}, using equally spaced N^{bins} bins of the size b (see Fig. 2.4). Each bin is assigned with a frequency of occurrence f_i^{exp} that can be normal-

ized with respect to the overall number of measurements as f_i^{exp}/N^{exp}. From that, we can compute the experimental probability density function (PDF) as a set of discrete values:

$$P_i^{exp} = \frac{f_i^{exp}}{N^{exp}} \cdot \frac{1}{b}. \tag{2.2}$$
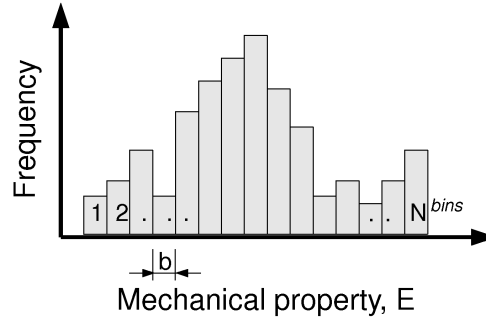
Figure 2.4: Construction of property histogram with bin size b.

The task of deconvolution into M phases represents finding $j = 1 \ldots M$ individual PDFs related to single material phases. If we assume normal (Gauss) distributions, the PDF for a single phase can be written as:

$$p_j(x) = \frac{1}{\sqrt{2\pi s_j^2}} exp \frac{-(x - \mu_j)^2}{2s_j^2} \tag{2.3}$$

in which μ_j and s_j are the mean value and standard deviation of the j-th phase computed from n_j values as:

$$\mu_j = \frac{1}{n_j} \sum_{k=1}^{n_j} x_k \qquad s_j^2 = \frac{1}{n_j - 1} \sum_{k=1}^{n_j} (x_k - \mu_j)^2 \tag{2.4}$$

and x is the approximated quantity, i.e. the E modulus in our case. The overall PDF covering all M phases is then:

$$C(x) = \sum_{j=1}^{M} f_j p_j(x) \tag{2.5}$$

where f_j is the volume fraction of a single phase:

$$f_j = \frac{n_j}{N^{exp}} \tag{2.6}$$

It was proposed to find individual distributions by minimizing the following error function:

$$min \sum_{i=1}^{N^{bins}} \left[\left(P_i^{exp} - C(x_i) \right) P_i^{exp} \right]^2 \tag{2.7}$$

in which quadratic deviations between experimental and theoretical PDFs are computed in a set of discrete points that is further weighted by the experimental probability in order to put emphasis on the measurements with a higher occurrence.

For practical computations, the number of mechanically distinct phases M must be known in advance to reduce the computational burden and to give the results a physical meaning. It is usually assessed by some independent measurements, using the knowledge of sample chemistry or simply by detection of several significant peaks in the property histogram. Also the bin size b have to be chosen in advance. Higher value of b leads to more fuzzy histograms with the peaks being smoothed whereas low value of b leads to more precise distributions but the distinctinon between the phases may be harder. In case of structural materials included in this work a reasonable bin size was find to be $b = 1$ GPa and the number of distinct phases M was 1 to 5 depending on a sample.

The minimization in Eq. (2.7) was based on the random Monte Carlo generation of M probability density functions. They have to satisfy the compatibility condition:

$$\sum_{j=1}^{M} f_j = 1. \tag{2.8}$$

There is an infinite number of possibilities that can satisfy the condition Eq. (2.8). So, completely random generation of the sets can lead to a time consuming procedure. In order to guarantee the convergence of the algorithm and to minimize the computational effort, it is suggessted in this work to use the set of M PDFs in Eq. (2.3) generated from the experimental dataset of all E moduli. Separation of the dataset into M randomly spaced successive intervals can be done in a straightforward way (see Fig. 2.5). Mean values, standard deviations in Eq. (2.4) and volume fractions in Eq. (2.6) are then computed in these intervals from corresponding E moduli and used in Eq. (2.5). Then, finding of the set satisfying condition Eq. (2.7) is a question of a few seconds on a regular PC.
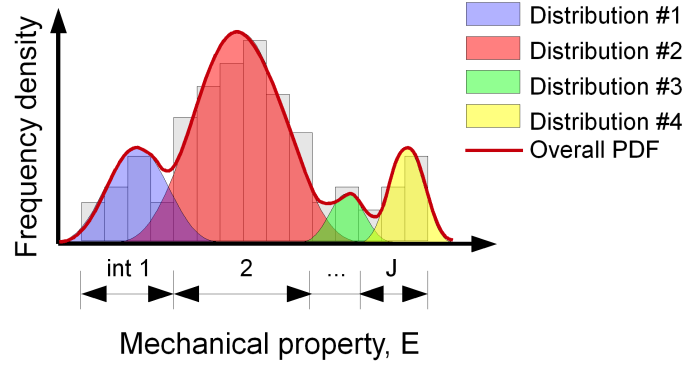
Figure 2.5: Separation of the experimental dataset to $j = 1 \dots M$ intervals and construction of M probability density functions.

2.4 Up-scaling of mechanical properties

Up-scaling of mechanical properties from microscale to the macroscopic level relies on homogenization techniques in which microscopically inhomogeneous body is replaced by a fictitious homogeneous one which behaves globally in the same way. Continuum mechanics uses mainly the concept of representative volume element (RVE) that obeys the scale separation condition Eq. (2.1) for a multilevel material. Preliminary results in the field of homogenization techniques were obtained for the first time by Voigt in 1887 who postulated the 'rule of mixtures' and in 1929 by Reuss (Reuss estimate). In early 1960s the basis of continuum micromechanics was found by Hill [30]. Continuum micromechanics seeks for the solution of the localization (or concentration) problem for a given spacial distribution of phases in RVE. The localization problem of the mechanical modeling of interactions between the phases which is associated with the local stress or strain fields $\boldsymbol{\sigma}(\mathbf{x})$, $\boldsymbol{\varepsilon}(\mathbf{x})$ is solved from global macroscopic stress and strain fields $\boldsymbol{\Sigma}$, $\boldsymbol{E}$ on the RVE. This problem cannot be solved in general, so additional assumptions need to be done in order to derive some estimates or bounds. Moreover, the boundary conditions are generally unknown so the problem is firstly transformed into simpler one by assuming homogeneous boundary conditions on the RVE [24, 25]. For the homogeneous boundary condition, tractions are prescribed as:

$$\boldsymbol{T}(\mathbf{x}) = \boldsymbol{\Sigma} \cdot \mathbf{n} \tag{2.9}$$

where $\mathbf{n}$ is the unit outward normal at the boundary, $\boldsymbol{T}(\mathbf{x})$ are the surface tractions and $\boldsymbol{\Sigma}$ is known macroscopic stress tensor. For any equilibrated

stress $\boldsymbol{\sigma}(\mathbf{x})$, the volume average stress $\langle\boldsymbol{\sigma}\rangle$ equals to $\boldsymbol{\Sigma}$ in the RVE of volume V:

$$\langle\boldsymbol{\sigma}\rangle = \frac{1}{V}\int_V \boldsymbol{\sigma}(\mathbf{x})dV = \boldsymbol{\Sigma}. \tag{2.10}$$

Similarly, a macroscopic strain can be associated to prescribed surface displacements $\mathbf{u}(\mathbf{x})$:

$$\mathbf{u}(\mathbf{x}) = \boldsymbol{E}\cdot\mathbf{x} \tag{2.11}$$

where $\boldsymbol{E}$ stands for macroscopic strain tensor and $\mathbf{x}$ determines the position at the boundary. For any strain field $\boldsymbol{\varepsilon}(\mathbf{x})$ obeying Eq. (2.11), the macroscopic strain reads:

$$\langle\boldsymbol{\varepsilon}\rangle = \frac{1}{V}\int_V \boldsymbol{\varepsilon}(\mathbf{x})dV = \boldsymbol{E}. \tag{2.12}$$

The homogeneous boundary conditions Eqs (2.9) and (2.11) lead to formulation of Hill's lemma for the strain energy density where at least strain or stress field satisfies homogeneous boundary conditions:

$$\langle\boldsymbol{\sigma}(\mathbf{x}):\boldsymbol{\varepsilon}(\mathbf{x})\rangle = \langle\boldsymbol{\sigma}(\mathbf{x})\rangle : \langle\boldsymbol{\varepsilon}(\mathbf{x})\rangle = \boldsymbol{\Sigma}:\boldsymbol{E}. \tag{2.13}$$

Further on, approximate microscopic stress or strain fields can be linked to macroscopic ones by using of strain or stress localization (concentration) tensors $\mathbf{A}(\mathbf{x})$, $\mathbf{B}(\mathbf{x})$. In case of linear elasticity it reads:

$$\boldsymbol{\varepsilon}(\mathbf{x}) = \mathbf{A}(\mathbf{x}):\boldsymbol{E}, \tag{2.14}$$

$$\boldsymbol{\sigma}(\mathbf{x}) = \mathbf{B}(\mathbf{x}):\boldsymbol{\Sigma}. \tag{2.15}$$

Because of Eqs (2.10) and (2.12):

$$\langle\mathbf{A}(\mathbf{x})\rangle = \langle\mathbf{B}(\mathbf{x})\rangle = \mathbf{I} \tag{2.16}$$

in which $\mathbf{I}$ is the forth-order symmetric unity tensor. Combining Eq. (2.10), Eq. (2.12) and Eq. (2.14), Eq. (2.15) with Eq. (2.13) one gets:

$$\boldsymbol{E}:\boldsymbol{\Sigma} = \langle\boldsymbol{\varepsilon}(\mathbf{x}):\boldsymbol{\sigma}(\mathbf{x})\rangle = \langle\boldsymbol{\varepsilon}(\mathbf{x}):\mathbf{B}(\mathbf{x}):\boldsymbol{\Sigma}\rangle, \tag{2.17}$$

$$\boldsymbol{\Sigma}:\boldsymbol{E} = \langle\boldsymbol{\sigma}(\mathbf{x}):\boldsymbol{\varepsilon}(\mathbf{x})\rangle = \langle\boldsymbol{\sigma}(\mathbf{x}):\mathbf{A}(\mathbf{x}):\boldsymbol{E}\rangle. \tag{2.18}$$

In principle, the Eqs (2.17) and (2.18) are not equivalent but tend to be so for sufficiently large sample.

Let us assume linear elastic constitutive relations for local fields:

$$\boldsymbol{\sigma}(\mathbf{x}) = \mathbf{c}(\mathbf{x}) : \boldsymbol{\varepsilon}(\mathbf{x}), \tag{2.19}$$

$$\boldsymbol{\varepsilon}(\mathbf{x}) = \mathbf{s}(\mathbf{x}) : \boldsymbol{\sigma}(\mathbf{x}) \tag{2.20}$$

where $\mathbf{c}(\mathbf{x})$ and $\mathbf{s}(\mathbf{x})$ are local stiffness and compliance tensors, respectively.

Inclusion of Eq. (2.14) into Eq. (2.19), Eq. (2.10) and Eq. (2.15) into Eq. (2.20), Eq. (2.12) reads effective stiffness and compliance tensor:

$$\boldsymbol{\Sigma} = \langle \boldsymbol{\sigma} \rangle = \frac{1}{V} \int_V \mathbf{c}(\mathbf{x}) : \mathbf{A}(\mathbf{x}) : \boldsymbol{E} dV = \boldsymbol{C}^{\textit{eff}} : \boldsymbol{E}, \tag{2.21}$$

$$\boldsymbol{E} = \langle \boldsymbol{\varepsilon} \rangle = \frac{1}{V} \int_V \mathbf{s}(\mathbf{x}) : \mathbf{B}(\mathbf{x}) : \boldsymbol{\Sigma} dV = \boldsymbol{S}^{\textit{eff}} : \boldsymbol{\Sigma}. \tag{2.22}$$

Because of heterogeneous sample is often expressed as a set of r phases with volume fractions f_r, it is beneficial to replace the integral in Eqs (2.21) and (2.22) with a summation as:

$$\boldsymbol{C}^{\textit{eff}} = \sum_r f_r \mathbf{c}_r : \mathbf{A}_r : \boldsymbol{E}, \tag{2.23}$$

$$\boldsymbol{S}^{\textit{eff}} = \sum_r f_r \mathbf{s}_r : \mathbf{B}_r : \boldsymbol{\Sigma}. \tag{2.24}$$

Various estimates of concentration tensors $\mathbf{A}_r$ or $\mathbf{B}_r$ can be obtained using Eshelby's solution of the inclusion-matrix problem [31]. Considering ellipsoidal inclusion embedded in an elastic matrix with the stiffness tensor $\mathbf{C}_0$ (the reference medium) the strain field $\boldsymbol{\varepsilon}_r$ in the inclusion is uniform if a homogeneous strain $\boldsymbol{E}$ is imposed in infinity. For ellipsoidal inclusion, the concentration tensor $\mathbf{A}_r$ takes the form:

$$\mathbf{A}_r^{est} = [\mathbf{I} + \mathbf{S}_r^{Esh} : (\mathbf{C}_0^{-1} : \mathbf{c}_r - \mathbf{I})]^{-1} : \left\langle [\mathbf{I} + \mathbf{S}_r^{Esh} : (\mathbf{C}_0^{-1} : \mathbf{c}_r - \mathbf{I})]^{-1} \right\rangle^{-1} \tag{2.25}$$

The Eshelby tensor $\mathbf{S}_r^{Esh}$ depends on the geometry and orientation of the phase. For a spherical inclusion and isotropic elasticity, the tensor composes of volumetric and deviatoric part as:

$$\mathbf{S}_r^{Esh} = \alpha_0 \mathbf{J} + \beta_0 \mathbf{K}, \tag{2.26}$$

$$\alpha_0 = \frac{3k_0}{3k_0 + 4\mu_0}, \beta_0 = \frac{6k_0 + 12\mu_0}{15k_0 + 20\mu_0} \tag{2.27}$$

in which k_0 and μ_0 are bulk and shear moduli of a reference medium and $\mathbf{J}$, $\mathbf{K}$ are volumetric and deviatoric parts of a unity tensor $\mathbf{I}$:

$$\mathbf{J}_{ijkl} = (1/3)\delta_{ij}\delta_{kl}, \mathbf{K} = \mathbf{I} - \mathbf{J} \qquad (2.28)$$

where δ_{ij} is the Kronecker delta. Similarly, the stiffness tensors of the phases and the homogenized material can be decomposed as:

$$\mathbf{c}_r = 3k_r\mathbf{J} + 2\mu_r\mathbf{K}, \qquad (2.29)$$

$$\mathbf{C}_{hom} = 3k_{hom}\mathbf{J} + 2\mu_{hom}\mathbf{K}. \qquad (2.30)$$

Finally, the relation between isotropic elastic constants can be useful for obtaining Young's modulus E and Poisson's ratio ν from bulk and shear moduli:

$$E = \frac{9k\mu}{3k + \mu}, \qquad (2.31)$$

$$\nu = \frac{3k - 2\mu}{6k + 2\mu}, \qquad (2.32)$$

$$k = \frac{E}{3(1 - 2\nu)}, \qquad (2.33)$$

$$\mu = \frac{E}{2(1 + \nu)}. \qquad (2.34)$$

Various estimates considering special choices of $\mathbf{C}_0$ can be found in literature trying to express at best the specific morphology of the material. For example, the rule of mixtures can be derived for vanishing $\mathbf{C}_0$, i.e. $\mathbf{A} = \mathbf{I}$. The Mori-Tanaka method [32] is devoted to composites with continuous matrix reinforced with discontinuous inclusions. In the self-consistent scheme [30] the reference medium points to the homogenized medium itself, thus the solutions takes the implicit form. This method is well suited for dispersed phases within RVE so none of them plays a significant morphological role. Other methods have been developed for layered spherical inclusions in a matrix [33] which can be successfully used e.g. for the homogenization of ITZ zones [34]. Upper and lower limits of the homogenized elastic constants are often estimated using bounds, such as *Voigt* and *Reuss* bounds, *Hashin-Strikman* [35] or *Hashin-Strikman-Walpole* bounds [36].

Cement-like composites usually obey the condition of morphologically significant matrix phase filled with differently shaped inclusions. The proper homogenization method can, therefore, be Mori-Tanaka scheme. It appears

also from other studies [10] that this scheme is a simple but effective homogenization tool that can be used on several material levels.

Besides the aforementioned analytical methods there are also many numerical homogenization methods searching for the stiffness tensor of the homogenized medium. These methods are usually based on the concept of eigenstrains [20], finite element computations [37, 38] or fast Fourier transformation [39, 36].

2.4.1   Mori-Tanaka homogenization scheme

The Mori-Tanaka scheme [32] assumes a composite to be characterized by the continuos morphologically prevailing matrix that is reinforced by distinct non-continuous inclusions (Fig. 2.6).
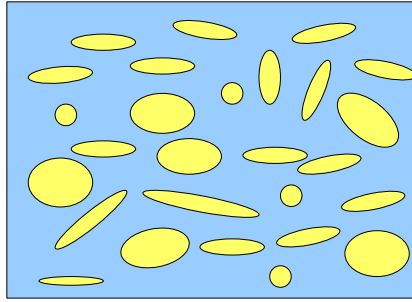
Figure 2.6: Matrix with particulate inclusions.

It takes into account the morphology, arrangements, volume fractions of the phases and interactions between the neighboring inclusions. Explicit estimates for isotropic matrix with spherical inclusions can be directly derived from Eqs (2.23) and (2.25) using Eqs (2.26) and (2.27). The results for the homogenized bulk and shear moduli then are:

$$k_{hom} = \frac{\sum_r f_r k_r \left(1 + \alpha_0(\frac{k_r}{k_0} - 1)\right)^{-1}}{\sum_r f_r \left(1 + \alpha_0(\frac{k_r}{k_0} - 1)\right)^{-1}}, \tag{2.35}$$

$$\mu_{hom} = \frac{\sum_r f_r \mu_r \left(1 + \beta_0(\frac{\mu_r}{\mu_0} - 1)\right)^{-1}}{\sum_r f_r \left(1 + \beta_0(\frac{\mu_r}{\mu_0} - 1)\right)^{-1}} \tag{2.36}$$

where subscript 0 denotes the reference medium and r particulate spherical phases, hence k_0 and μ_0 are bulk and shear moduli of a reference medium

and k_r and μ_r refer to inclusion phases . Homogenized Young's modulus and Poisson's ratio are then:

$$E_{hom} = \frac{9k_{hom}\mu_{hom}}{3k_{hom} + \mu_{hom}}, \tag{2.37}$$

$$\nu_{hom} = \frac{3k_{hom} - 2\mu_{hom}}{6k_{hom} + 2\mu_{hom}}. \tag{2.38}$$

Chapter 3

Analysis of structural materials

Nanoindentation and the methodology described in previous sections will be demonstrated on several types of typical heterogeneous structural materials: cement paste, two types of alkali-activated fly ashes (AAFAs) and metakaolin. Cement paste was chosen to represent a group of classical cement-based composites. Nowadays, cement and concrete are probably the mostly used building materials whose environmental impact is enormous. Therefore, investigations on cement properties, behavior and its numerical modeling on all scales is desirable.

AAFAs represent a new emerging group of alternative aluminosilicate materials that can be possibly used for partial replacement of ordinary Portland cements. Metakaolin is a kind of homogeneous-like solid compared to the first two and was chosen for comparison purposes and to show some mutual similarities between aluminosilicates in general.

3.1   Sample preparation

The key issue of any experimental technique is the sample preparation. Both nanoindentation and ESEM are very sensitive to it. In case of nanoindentation, the data analysis assumes sample to have a flat surface and to be indented in a perpendicular direction (Fig. 1.13). Similarly, a rough sample surface can lead to dispersion or loss of a signal in electron microscope. Proper conditions can only be achieved using careful mechanical procedures. In our case, samples were cut to parallel slices of ≈ 5 mm in thickness by a precision diamond saw and dried. Then, polished on fine emery papers and polishing cloth, and cleaned in an ultrasonic bath to clear the pores from dust and removed particles.

In order to guarantee reliable results from nanoindentation the roughness

of the sample surface should be checked for its profile by atomic force microscope (AFM), for instance. The roughness parameters must always by compared to the expected final penetration depths. In our case, the average depth around 200 nm was expected, so the roughness $\approx$ 20 nm was desirable. Since the indent is always placed over a small area (around 1 μm), local roughness characteristics are sufficient. The sample preparation is illustrated in Fig. 3.1 where AFM images of cement paste after diamond saw cutting and after final polishing are shown. Local roughness characteristics on at least ten randomly selected areas 30 $\times$ 30 μm were computed. So called root-mean-square parameter was used for the roughness quantification [40]. It is defined as:

$$RMS = \sqrt{\frac{1}{M \times N} \sum_{i=1}^{M} \sum_{j=1}^{N} h_{ij}^2} \qquad (3.1)$$

where M and N stand for the number of measured heights h_{ij} in two perpendicular directions i and j, respectively. For cement paste, the RMS parameter after diamond saw cutting was 558 ± 165 nm and after final polishing 25 ± 6 nm.
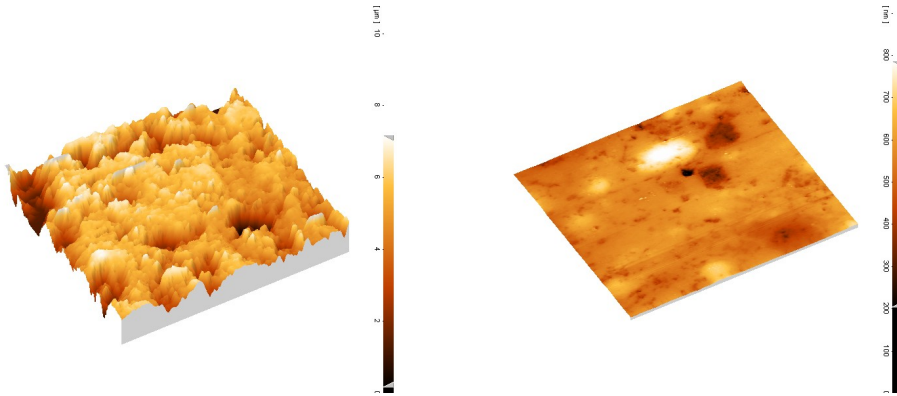
Figure 3.1: AFM images of the surface roughness after diamond saw cutting (left) and after polishing (right).

3.2 Indentation strategy

Due to the varying heterogeneous composition of all samples, several (at least three) representative areas were selected on each sample. Nanoindentation was carried out in a series of grids having typically $10 \times 10 = 100$ imprints in

each area. The distance between individual indents varied in measurements in order to cover the heterogeneity of the sample. It was prescribed in the range of $10 - 50$ μm. All together, around 400 imprints were carried out for cement paste sample, around 700 for each AAFA sample and around 500 for metakaolin.

3.3 Cement paste

Cement paste, i.e. cement powder mixed with water, is a typical representative of a multiscale material which evolves during hydration process and, in presence of water, for many years. When the cement is mixed with water, hydration reactions occur which convert the suspension into a rigid porous material. As known from cement chemistry, the basic building unit in hydrated cement matrix consists of calcium-silica-hydrates (C-S-H gels). C-S-H appears in many morphological forms. Its now also agreed by many researchers that C-S-H exists in two mechanically distinct phases that are denoted further as low- and high-density C-S-H gels. The two C-S-H types differ in the packing densities of their basic building blocks called globules. The morphology of the high-density C-S-H corresponds to closely packed globules while low-density C-S-H is characterized by randomly-packed spheres [41]. In later stages of an induction period of hydration, calcium hydroxide (CH, Portlandite) appears and is incorporated into hydrated mass in the form of crystals within the pores as well as dispersed amorphous parts. An important part of the developing solid is also a capillary porosity and the rest of unhydrated raw material, the clinker.

The microstructure of hydrated cement paste is shown in Fig. 3.2. Backscattered electrons of ESEM image clearly mark the areas with different densities which correspond to basic components. The very light areas in Fig. 3.2 belong to unhydrated clinker, light grey areas are mostly rich of Portlandite and dark grey colors represent C-S-H. Black spots are places with very low or zero density, so basically mechanically weak areas and pores.

3.3.1 Material and curing of cement samples

Portland cement CEM-I 42,5R originating from Mokrá, the Czech Republic was used in this study. The fineness of the cement, characterized by the Blaine specific surface, was 306 m^2kg^{-1}. The chemical composition of the raw clinker is given in Tab. 3.1 and particle size distributions in Fig. 3.3. Cement was mixed in water–cement ratio w/c=0.5 by weight and cured in water for 1 year. After one year in water, almost full hydration occurs and
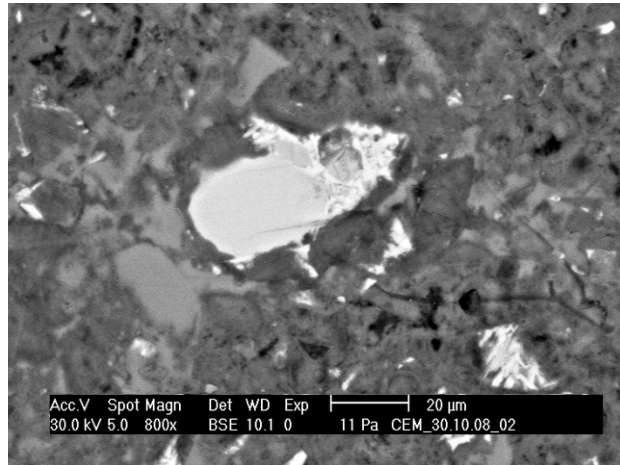
Figure 3.2: ESEM (BSE) image of hydrated cement paste.

only large clinker grains remain unhydrated in the matrix. The degree of hydration estimated by Cemhyd3D model [42] was 92% for this particular case.

Table 3.1: The chemical composition of raw cement (wt. %)

Component	CaO	SiO$_2$	Al$_2$O$_3$	Fe$_2$O$_3$	MgO	TiO$_2$
wt. %	63.77	20.51	4.74	3.3	1.05	0
Component	K$_2$O	Na$_2$O	SO$_3$	MnO	free Ca	
wt. %	0.95	0.15	3.07	0.09	0	
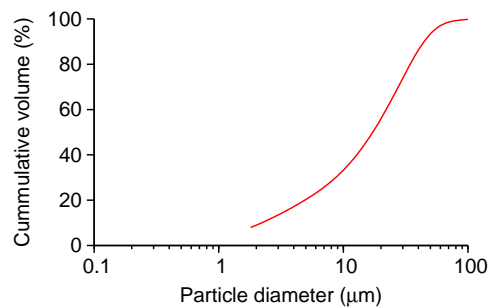
Figure 3.3: Particle size distribution of cement CEM-I 42,5R, Mokrá.

3.3.2 Statistical nanoindentation

Nanoindentation measurements were performed in a load control regime using the Hysitron Tribolab System with a Berkovich tip. The trapezoidal loading diagram was prescribed for all tests (Fig. 3.4). Linear loading of 12 mN/min and lasting for 10 s produced a maximum load of 2 mN for all indents. The holding period (30 s) under the constant force followed, allowing material to creep. This stage is important for unbiasing the unloading stage [1]. The following unloading branch of 12 mN/min for 10 s was supposed to be purely elastic. The applied peak load of 2 mN led to maximum penetration depths ranging from 100 nm to 400 nm (average 220 nm) depending on the hardness of the indented material phase. The effective depth captured by the tip of the nanoindenter can be roughly estimated as three times of the penetration depth for the Berkovich indenter [26]. It yields the effective depth of around 1 μm for this particular case. Nanoindentation response obtained for different material components is depicted in Fig. 3.5 and it clearly shows on different deformations and stiffnesses of distinct phases if the same load is applied. Elastic properties were evaluated from nanoindentation tests according to the Oliver-Pharr methodology [14].
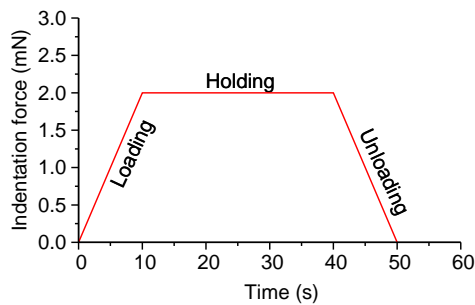
Figure 3.4: Prescribed loading diagram in indentation experiments.
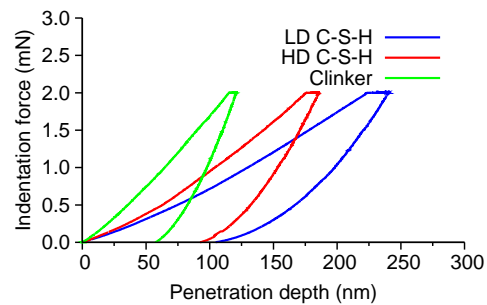
Figure 3.5: Example of load-penetration curves obtained for distinct phases on cement samples by nanoindentation.

Due to the heterogeneity of the material individual grid results depend very much on the location and indents' spacing. As observed in ESEM, the heterogeneity occurs on the scale of tens or even hundreds of μm. This fact has been confirmed also by nanoindentation where one can find differences between individual grids with spacing 10–50 μm as shown in Fig. 3.6. In Fig. 3.6 the grid #1 lay in the area rich of soft LD C-S-H, grid #2 covers basically all phases and grid #3 contains also all phases with the slight shift

towards stiffer phases (HD C-S-H and CH).

Overall results of reduced elastic moduli of cement paste samples (≈ 400 indents) are merged and plotted in Fig. 3.7. The large number of indents and also large area covered by nanoindentation is necessary to receive results for all phases. The experimental histogram covers all these phases including their intrinsic porosity. They are denoted in the plot as:

A. Low stiffness phases – phases with $E_r \leq 10$ GPa

B. Low density C-S-H

C. High density C-S-H

D. Portlandite (CH)

E. Unhydrated rest of clinker minerals

The deconvolution into the aforementioned phases has been carried out with the assumption that values of E_r higher then ≈ 50 GPa can be attributed to residual unreacted cement clinker grains and they were not considered in the deconvolution.
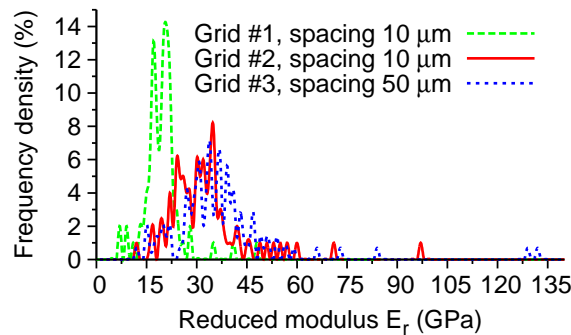
Figure 3.6: Histogram of reduced moduli for three different indentation grids on a cement paste sample

The results are summarized in Tab. 3.2. They can be directly compared with results from literature, e.g. Constantinides et al. [10, 22]. Generally, very good agreement was achieved in terms of reduced moduli which together with their standard deviations overlap for individual phases and also the frequency of occurance of distinct phases is comparable.
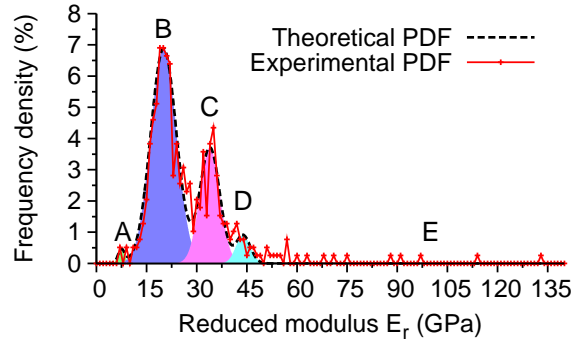
Figure 3.7: Overall experimental and theoretical probability density functions with segmented four phases in cement paste samples.

Table 3.2: Reduced moduli E_r (GPa) of individual material phases in cement paste from this study and comparison with literature results. The values in parentheses denote frequency of occurance.

	Reduced modulus E_r (GPa) and frequency of occurance (%)		
Phase	**This study**[1]	Literature [10] [2]	Literature [22] [3]
A. Low stiffness	**7.45 $\pm$ 0.98** (1.05 %)	n/a	8.1 $\pm$ 1.7 (6 %)
B. LD C-S-H	**20.09 $\pm$ 3.85** (63.17 %)	21.7 $\pm$ 2.2 (67 %)	18.2 $\pm$ 4.19 (51 %)
C. HD C-S-H	**33.93 $\pm$ 2.98** (26.34 %)	29.4 $\pm$ 2.4 (33 %)	29.1 $\pm$ 4.07 (27 %)
D. Portlandite	**43.88 $\pm$ 2.15** (4.61 %)	n/a	40.3 $\pm$ 4.03 (11 %)
E. Non-hydrated	n/a (4.83 %)	n/a	n/a

[1] CEM-I 42,5R, w/c=0.5, cured in water for 1 year. Results taken from 400 indents from four sample locations covering at least 10×10 μm each.
[2] Portland cement Type I, w/c=0.5, cured in a saturated lime solution for 27 days. Results taken from 200 indents covering an area of 1000 μm [2].
[3] White Portland cement, w/c=0.5, cured in lime water for 5 months. Results taken from 300 indents covering an area of 10×10 μm each.
n/a ... Not available from the study.

3.3.3 Pointed nanoindentation

As discussed in Section 2.2 there are several possibilities to access material properties by nanoindentation on different scales. Probably the most effective one is the pointed nanoindentation into a specific material phase provided it can be distinguished in microscope and the indenter can be focused on the area of interest. On cement paste samples this is not a case because the phases

are intermixed in hydration compound and the distinction cannot be based just on the color differences as seen in optical microscope or BSE images of ESEM. But there are basically two exceptions:

(i) Clinker

The clinker can be easily recognized morphologically as odd-shaped grains or very light areas in BSE images (see Figs 3.2 and 3.8). But their direct indentation on cement paste specimen poses the difficulty that it is surrounded by relatively soft matrix and it 'floats' in it. Therefore their mechanical response is affected by this fact and usually smaller stiffnesses ($E \leq 100$ GPa) are obtained from nanoindentation than would be appropriate (125-145 GPa [9]). The stiffness mismatch ratio for the clinker and matrix can be roughly estimated as:

$$\frac{E_{LD-CSH}}{E_{clinker}} \approx \frac{20GPa}{135GPa} \approx 0.15. \tag{3.2}$$

It is clear that the ratio exceeds the interval $[0.2, 5]$ discussed in Section 2.2. If intrinsic properties of clinker are of the interest than direct measurements out of the cement paste need to be performed.

(ii) High-density C-S-H

On the level of cement grains, the high-density C-S-H zones tend to develop in their closest neighborhood [43]. This effect can be recognized in BSE images as a closed or partly closed rim around the cement grains with a dark grey color compared to the ground hydrated mass (see Fig. 3.8). For a typical large cement grain (10-20 μm) in cement paste the HD C-S-H zone can be of $\approx 5 - 10$ μm thickness. Thus, this zone is large enough to be indented by pointed indentation whose effective depth is smaller then 1/10 of the layer thickness (i.e. ≤ 1 μm).

3.3.4   Nanoindentation on cement clinker

The assessment of intrinsic elastic properties of a cement clinker using pointed nanoindentation was proposed on samples of dry polished clinker. The grain of an industrial cement clinker taken at the cement works was first embedded in dentacryl poured to the cylindrical mould. Then it was cut in the middle and the surface was dry polished to achieve a roughness less than ≈ 50 nm. Industrial cement clinker is a compound of different natural minerals. There are two major constituents called Alite and Belite (these minerals can
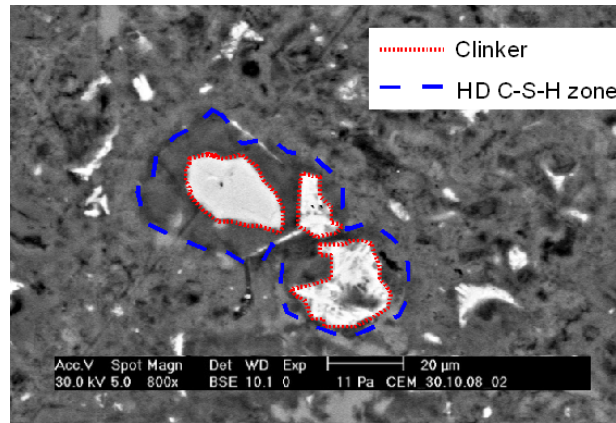
Figure 3.8: ESEM (BSE) image of hydrated cement paste with distinction of unhydrated relict of a clinker grain surrounded by the HD C-S-H zone.

contain some degree of impurity). They are related to pure chemical phases – tricalcium silicate (C_3S) and dicalcium silicate (C_2S). Further, tricalcium aluminate (C_3A) and calcium aluminoferrite (C_4AF) can be present in a clinker [16, 17]. Our sample was taken directly from the cement works and thus it consisted of a mix of these phases. Using the EDX analysis in ESEM it was determined that the places used for subsequent indentation were created mainly by Belite (C_2S) and, therefore, results were computed for this particular mineral phase.

The matrix of 80 indents (Fig. 3.9) was prescribed to the maximum load 10 mN (loading at 0.3 mN/s, 200 s holding period and unloading at 0.3 mN/s) as shown in Fig. 3.10. Negligible creep behavior was observed during the holding period at peak load (Fig. 3.11). From that it can be concluded that unhydrated clinker is not responsible for the time-dependent behavior of cement paste but hydrated products. Indentation modulus of the indented phase of clinker, i.e. Belite (C_2S), was determined as $E_r = 113 \pm 11$ GPa. Using the assumption of Poisson's ratio 0.2 leads to the elastic modulus $\boldsymbol{E = 121 \pm 14}$ **GPa** which is in a very good agreement with literature results (see Velez et al. [9] : $E_{C_3S} = 135 \pm 7$ GPa, $E_{C_2S} = 130 \pm 20$ GPa, $E_{C_3A} = 145 \pm 10$ GPa, $E_{C_4AF} = 125 \pm 25$ GPa, $E_{Alite} = 125 \pm 7$ GPa and $E_{Belite} = 127 \pm 7$ GPa).

3.3.5 Nanoindentation on high-density C-S-H

The high-density C-S-H gel zones were identified in ESEM (Fig. 3.13), in optical microscope (Fig. 3.12) and located by nanoindenter. Over 80 indents
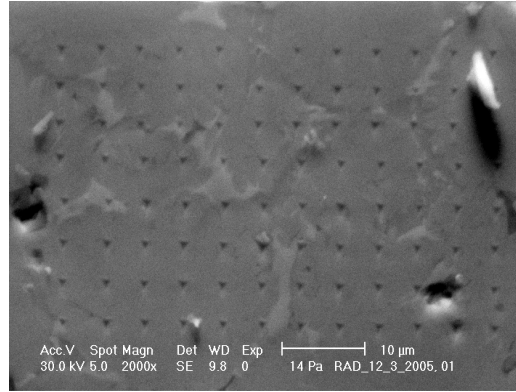
Figure 3.9: ESEM (BSE) image of cement clinker with indentation matrix.
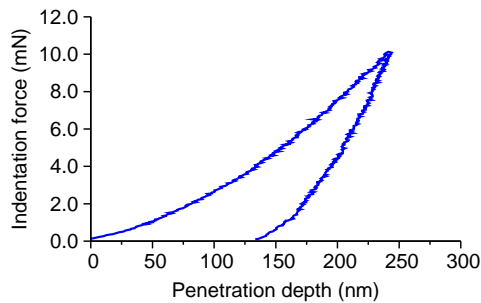
Figure 3.10: Loading diagram of clinker (belite).
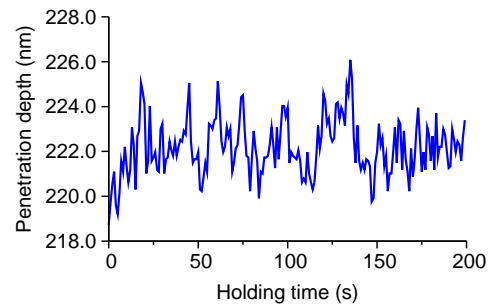
Figure 3.11: Evolution of the depth of penetration during holding period (at constant peak load).

were placed around arbitrarily chosen clinker grains. Loading was prescribed to the maximum load 2 mN (at 12 mN/min) then 60 s long holding period and unloading at 12 mN/min) followed as can be seen in Figs 3.14 and 3.15.

Results merged from all indentations lead to the reduced modulus $\boldsymbol{E_r =}$ $\boldsymbol{38.605 \pm 2.569}$ **GPa** as depicted in Fig. 3.16. These results seem to be a bit higher than those obtained from statistical nanoindentation (in Section 3.3.2, $E_r = 33.93 \pm 2.98$ GPa). The reason can be that statistical indentation covers all areas also between cement grains and not only around them. The close vicinity of the clinker can also cause a local stiffening. But generally, the results are quite comparable.

Figure 3.12: High-density C-S-H zone with prescribed indents as seen in optical microscope of CSM nanohardness tester.
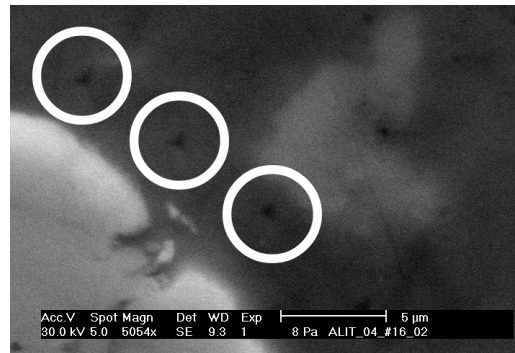
Figure 3.13: High-density C-S-H zone with performed indents as seen in ESEM).
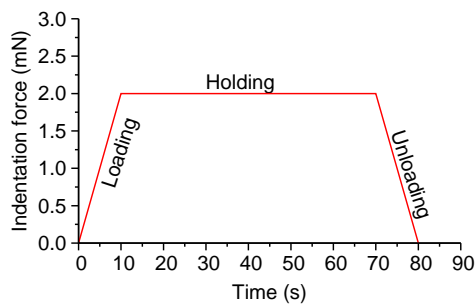
Figure 3.14: Prescribed loading diagram for HD C-S-H.
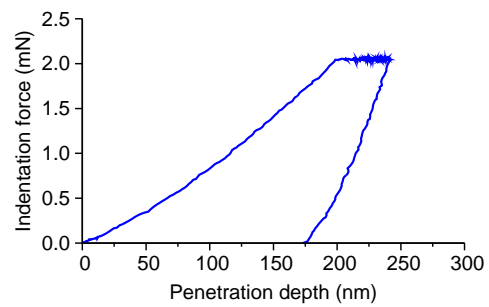
Figure 3.15: Example of load-penetration curve obtained for HD C-S-H.
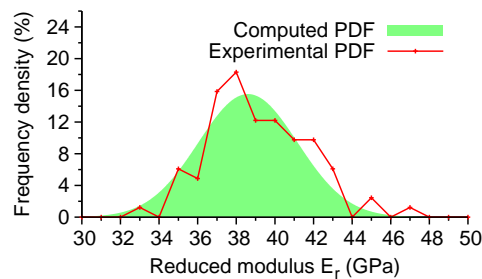
Figure 3.16: Overall experimental and computed probability density functions for HD C-S-H.

3.3.6 Homogenization of elastic properties on cement paste

The heterogeneous character of the microstructure of cement paste and the multiscale character of related composites like concrete has already been demonstrated in previous sections in some details. In order to assess effective elastic properties for higher levels of the composite from its microlevel homogenization techniques can be employed (Section 2.4). The scale separation condition Eq. (2.1) can be used to define the following scales:

- **Level 1** (C-S-H level) is being considered as the lowest level accessible by mechanical testing. The mechanically bimodal structure (low- and high-density) of C-S-H is expected at the scale of $d = 10^{-8} - 10^{-6}$ m. Nanoindentation results obtained in this study take place on $h \approx 10^{-6}$ m . The RVE size of the C-S-H level than can be at least ten times d, i.e. $L \approx 10^{-5}$ m which corresponds to observations of the cement matrix done in ESEM, for example. It is worth noted that this level necessarily includes also intrinsic nanolevel porosity of C-S-H as well as possible nanocrystaline phases, such as Portlandite, that mechanically interact with C-S-H. Therefore, the distinction of the mechanical phases, done for example by statistical nanoindentation, does not need to coincide with pure chemical phases.

- **Level 2** (Cement paste level) already includes large Portlandite (CH) crystals, unhydrated cement clinker and capillary porosity with characteristic sizes $d = 10^{-6} - 10^{-4}$ m which yield the RVE size of about $L = 10^{-4} - 10^{-3}$ m. Results from nanoindentation will include the first three mentioned phases but the porosity. This phase cannot be sufficiently discovered by mechanical means. But as in case of level 1, the homogenization uses mechanically distinct phases more that chemically of morphologically distinguishable ones. Therefore, the mechanical phases involved in the homogenization on this level will include homogenized C-S-H matrix (level 1), low stiffness phases, Portlandite and clinker phase as obtained from nanoindentation (Section 3.3).

- **Level 3** (Mortar level) refers to the three phase composite consisting of cement paste matrix, sand aggregate and interfacial transition zone (ITZ) between the matrix and inclusions. The characteristic dimension of the RVE is $L = 10^{-3} - 10^{-1}$ m for this scale.

- **Level 4** (Concrete level) takes into account the mortar, large aggregates and again the ITZ between the phases. The RVE in this case is $L = 10^{-1} - 10^{1}$ m.

Since nano/micromechanical studies are of primary interest in this work, homogenization will be performed for the first two levels here, i.e. up to cement paste level, as depicted in Fig. 3.17. It follows from the literature that the Mori-Tanaka [10] or self-consistent scheme [44] can be succesfully applied for this case. The Mori-Tanaka analytical scheme (Section 2.4) will be used in the following.
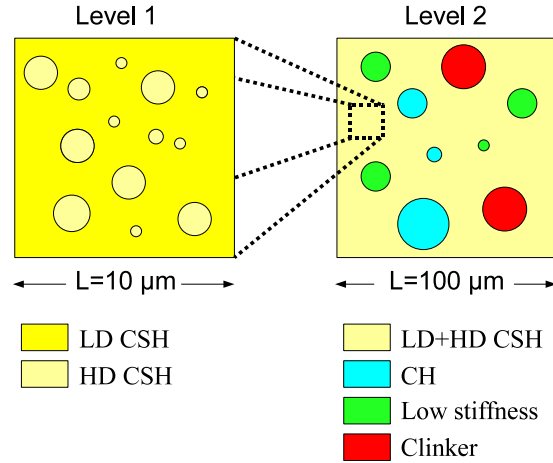
Figure 3.17: Separation of the composite to two levels: 1. C-S-H level and 2. cement paste level.

The input and output data for the C-S-H level and cement paste level homogenizations are summarized in Tab. 3.3 and Tab. 3.4, respectively. The reduced moduli E_r and volume fractions f_r are taken directly from nanoindentation results in Section 3.3. Poisson's ratii ν are estimated from the open literature.

Table 3.3: Input data and results of homogenization for the C-S-H level.

	Phase	$E_r(GPa)$	ν	f_r
Input	LD C-S-H	20.09	0.2	0.706
	HD C-S-H	33.93	0.2	0.294
Output	Homogenized C-S-H	**23.363**	0.2	1

It can be seen from the results that the homogenized properties of cement paste are mainly dependent on the C-S-H properties and minor influence can be attributed to other phases. The clinker phase could potentially have large

Table 3.4: Input data and results of homogenization for the cement paste level.

	Phase	$E_r(GPa)$	ν	f_r
Input	C-S-H	23.363	0.2	0.8951
	Low stiffness	7.45	0.2	0.0105
	CH	43.88	0.3	0.0461
	Clinker	113	0.3	0.0483
Output	Cement paste	**25.343**	0.21	1

influence due to its high stiffness compared to C-S-H but at this later stage of hydration (one year old samples) the volume fraction is very low and thus the influence is low as well.

3.3.7 Conclusions

- Statistical indentation was applied on cement paste samples in order to evaluate intrinsic material properties of its distinct mechanical phases. According to cement chemistry four basic phases of hydration products, namely low stiffness phases, low- and high-density C-S-H gels and Portlandite were identified from property histograms capturing the heterogeneity of the specimen. Intrinsic phase properties identified in this study were in good agreement with literature results [10, 22].

- Results and differences found on individual indentation grids show on high degree of heterogeneity that exceeds the range of one grid, i.e. 100 μm.

- Indentation on cement clinker showed that unhydrated relicts of clinker minerals in cement paste are not responsible for its time-dependent behavior (creep) but the hydrated products.

- Due to the high stiffness mismatch ratio reliable results of clinker's intrinsic properties were obtained from direct measurement on non-hydrated clinker and not from hydrated cement paste.

- Pointed nanoindentation to high-density C-S-H located around unhydrated cement grains revealed slightly higher values of reduced moduli compared to statistical indentation which can be probably attributed to locally higher stiffnesses around the clinker.

- Elastic homogenization performed on cement paste level showed on high dependence on the C-S-H properties and its content in the sample. This can be directly attributed to the low volume fraction of high stiffness phases (clinker) for this particular case of one year old specimen.

3.4 Alkali-activated fly ash and metakaolin

A group of alkali-activated aluminosilicate materials draws the attention of researchers worldwide, see [45, 46] for a review. In comparison with conventional Portland cement-based composites these materials generally exhibit excellent durability, fire-resistance, but may suffer from efflorescence, shrinkage, inconvenient quality control or mastering the technology [47].

In the past, various raw materials (slag, fly-ash, metakaolin, clay) were intermixed with strong alkaline solutions to synthesize a poorly crystallized inorganic gel binder [48]. Coined nomenclatures such as 'soil cement' [49], 'geopolymer' [50] or 'inorganic polymer' [46] have characterized more or less similar dissolution-precipitation processes taking place in a strong alkaline environment due to different starting materials. Here, the term N-A-S-H gel (aluminosilicate gel) will describe a binding matrix phase, embedding undissolved inclusions of remaining raw material.

In the past, alkali-activated materials were characterized by a variety of experimental techniques including FTIR, ESEM, MAS-NMR, XRD, DTA or calorimetry [48, 51]. The majority of experimental data were linked directly to the atomic scale and nanostructure of N-A-S-H gel. However, all the above mentioned techniques suffer from data down-scaling by several orders of magnitude to the nanostructure of N-A-S-H gel. With this respect, nanoindentation sensing technique enables direct characterization of intrinsic mechanical properties on the micrometer and submicrometer resolution. The response is obtained directly from the close vicinity of a small indent without the interaction of distant material. A comprehensive study of intrinsic elastic properties of alkali-activated materials has never been performed in this field, although a few attempts can be found [52].

To shed light on different origins of N-A-S-H gel, both fly ash and metakaolin were activated under different curing temperatures. N-A-S-H gel appears as the main binding phase in both alkali-activated fly ash (AAFA) [53] and metakaolin (AAMK) [54], but mutual nanomechanical comparison has never been performed. The NMR and SEM analysis revealed that reaction products are structurally analogous in both materials [46]. Nanoindentation supports this hypothesis; intrinsic elastic properties of mature N-A-S-H gels were found to be independent of the curing temperature and activated materials as will

be shown later.

3.4.1   Materials, activation and curing of samples

Low calcium fly ash, class F, was obtained from the brown coal power plant Chvaletice, the Czech Republic. The Blaine specific surface was 210 m^2kg^{-1}. The fly ash was ground in a small-scale ball mill to crush hollow cenospheres and to facilitate the reduction in porosity. The XRD Rietveld analysis found the composition consisting of 70 vol. % amorphous phases, 24 vol. % mullite and 6 vol. % quartz.

Metakaolin originated from České lupkové závody a.s., Nové Strašecí, the Czech Republic. Chemical compositions of both materials are given in Tab. 3.5 and particle size distributions in Fig. 3.18.

Table 3.5: The chemical composition of ground fly ash and metakaolin (wt. %).

	SiO_2	Al_2O_3	Fe_2O_3	CaO	TiO_2	K_2O
Ground fly ash	51.9	32.8	6.3	2.7	1.89	2.12
Metakaolin	48.66	47.41	1.33	0.03	1.99	0.15
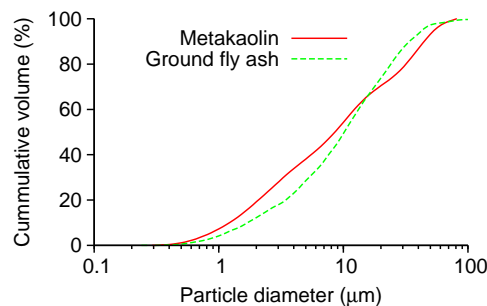
Figure 3.18: Particle size distribution of ground fly ash and metakaolin.

The alkali-activator was previously optimized to yield a high compressive strength while maintaining workability [51]. The activator was prepared by dissolving NaOH pellets in tap water and adding sodium waterglass. Tab. 3.6 summarizes the compositions of the mixtures. The final properties of the mixture can be controlled by three independent parameters (Tab. 3.6). Metakaolin requires significantly more activator due to its higher surface area.

Fly ash or metakaolin was intermixed with the activator for 5 minutes, cast in plastic ampules 26 mm in diameter and 45 mm in height, gently vibrated for 5 minutes and sealed. Heat-cured fly ash or metakaolin samples were exposed to 80°C for 12 hours. Ambient-cured fly ash experienced a laboratory temperature $\approx$ 22°C for the duration of six months prior to testing. Both materials are considered to be mature, although polymerization and hardening will never stop as known as aging from cement chemistry [16]. After a half-year from casting the compressive strength of AAFA samples exceeds 70 MPa and that of AAMK 50 MPa.

Table 3.6: Mixture composition. Mass oxide ratii for activators and activator-to-solid mass ratii.

	Activator ratii		Activator to
	Na_2O/SiO_2 (-)	H_2O/Na_2O (-)	solid ratio (wt. %)
Ground fly ash	0.881	3.925	0.531
Metakaolin	1.669	2.743	1.416

3.4.2 Nanoindentation

Samples were prepared similarly to cement paste samples and tested by the same methodology. Nanoindentation measurements were performed in a load control regime using the CSM Nanohardness tester equipped with a Berkovich tip. The loading diagram prescribed for all tests (Fig. 3.19) was characterized by linear loading of 4 mN/min (lasting for 30 s), holding period (30 s) and the unloading branch of 4 mN/min for 30 s. The peak load of 2 mN led to maximum penetration depths ranging from 100 nm to 400 nm (average 260 nm) depending on the hardness of the indented material phase so the effective depth was, similarly to cement, again around 1 μm for this case. Nanoindentation loading response obtained for material components with different mechanical stiffnesses is shown in Fig. 3.20. Elastic properties were evaluated from nanoindentation tests according to the Oliver-Pharr methodology [14]. Elastic modulus was computed from Eq. (1.6) assuming Poisson's ratio ν to be 0.2 for all measurements.

3.4.3 Porosity characterization

AAFA and AAMK samples were crushed to the size of a few millimeters, dried at 105 °C for 6 hours and intruded by mercury (MIP, Autopore III Mi-
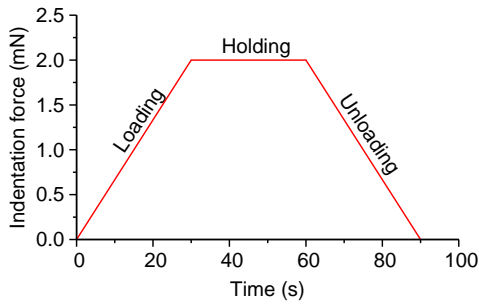
Figure 3.19: Prescribed loading diagram in indentation experiments.
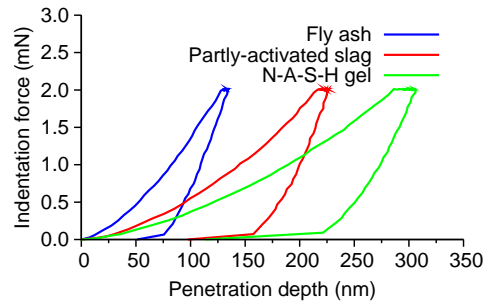
Figure 3.20: Example of load-penetration curves obtained for distinct phases on AAFA samples by nanoindentation.

cromeritics) or measured by He-pycnometry (Micromeritics AccuPyc 1330). The combination of MIP and He pycnometry allows estimating the 'total' porosity from bulk and skeletal densities:

$$\pi = \frac{\rho_{He}^{skeletal} - \rho_{Hg}^{bulk}}{\rho_{He}^{skeletal}}. \tag{3.3}$$

Both methods have their resolution limits; the size of a helium atom (d≈ 0.062 nm) from the bottom range and the limit of MIP from the top (d≈ 120 μm). Nevertheless, pore sizes of AAFA and AAMK samples fit well within both limits. The pore size distribution obtained from MIP is depicted in Fig. 3.21.
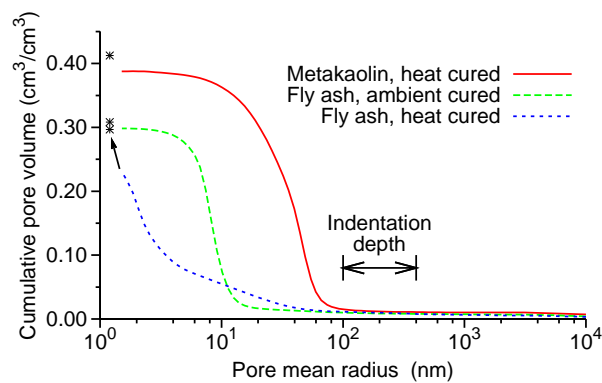
Figure 3.21: Cumulative pore volume measured by MIP. Asterisk denotes total pore volume determined from Eq. (3.3).

3.4.4   Results and discussion

AAFA and AAMK porosity

Fig. 3.21 testifies that a different curing temperature changes the distribution of pores but preserves the total porosity in AAFA samples. This coincidence probably implies the same reactions stoichiometry but with different reaction kinetics. Under an ambient curing temperature, AAFA remains in a quasi-liquid state for several days. During this period, N-A-S-H gel experiences slow polycondensation and syneresis with negligible mechanical restraint. Released water from polycondensation is expelled from the gel while forming larger pores [55, 56]. From a series of observations, ambient-cured samples generally exhibit much larger autogeneous shrinkage as opposed to heat-cured specimens.

The indentation depth lies above the maximum pore size, Fig. 3.21. This is partially contradicted by ESEM images in Figs 3.22 and 3.26 which show porosity on a micrometer range. Such a discrepancy is explained as the bottleneck effect which is controlled by fine-pore N-A-S-H gel. Careful avoidance of areas with large pores is a prerequisite for successful nanoindentation. Then, porosity is assumed to occupy the scale below the indentation depth hence nanoindentation tests characterize phases including their characteristic porosity from a lower scale.

ESEM and nanoindentation of heat-cured AAFA

Fig. 3.22 presents a characteristic structure of heat-cured AAFA formed from relics of bullets of iron and/or iron oxides and compact Si-Al glass. It is estimated that roughly a half of fly ash was transformed to N-A-S-H gel [57].

Other ESEM observations led to the conclusion that the AAFA heterogeneity occurs not only on a micrometer range but also on the scale of hundreds of μm, far exceeding the size of fly ash particles. This hypothesis was confirmed experimentally by nanoindentation. Three different representative regions were indented in three grids with different indent spacing. Fig. 3.23 shows that grids #1 and #2 lay in the areas rich in soft N-A-S-H gel while grid #3 hit the area of less activated fly ash with higher moduli.

Overall nanoindentation results from heat-cured AAFA samples (≈ 700 indents) are merged and plotted in Fig. 3.24. The histogram covers all phases, namely reaction products (N-A-S-H gel, partly-activated slags), including intrinsic porosity and unreacted fly ash (unreacted slags and glass particles). Based on thorough argumentation, four peaks in Fig. 3.24 were denoted and abbreviated as:

Figure 3.22: AAFA heat-cured polished samples in SE (left) and BSE (right). In BSE image appear white iron and/or iron oxides bullets (intact), and compact Si-Al glass. The spotted light grey particles are the remnants of alkali-activated Si-Al-Na-K fly ash. The original slag particles were dissolved and transformed to dark grey compact matter of N-A-S-H gel. The black spots are capillary pores.

Figure 3.23: Histogram of elastic moduli for three different indentation grids on a heat-cured AAFA sample.
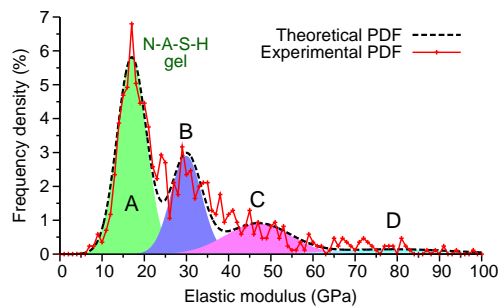
Figure 3.24: Overall experimental and theoretical probability density functions with segmented four phases in heat-cured AAFA samples.

A. **N-A-S-H gel** – pure N-A-S-H gel

B. **Partly-activated slag** – N-A-S-H gel intermixed with slag-like particles

C. **Nonactivated slag** – Porous nonactivated slag-like particles

D. **Nonactivated compact glass** – Solid nonactivated glass spheres or their relicts after grinding

The alkaline activation of fly ash is essentially a selective process caused by a significant heterogeneity in the composition of raw fly ash [57]. The ability and kinetics of the reaction depends not only on the chemical and/or mineralogical composition of fly ash but predominantly also on the internal structure of the particle, and especially on the specific surface area. The observations show that preferential and rapid activation takes place in the slag-like, large size, Si-Al [Na, K, Mg, Fe, Mn] particles with a rich hollow structure on the micro level, and Fe-Mg [Si-Al] large slag particles [51]. The last two particles are easily dissolved and transformed to N-A-S-H gel.

In order to support the proposed phase assignment, nanoindentation focused on partly-activated slag and compact glass particle. Indents were located in a row coming from the outbound particle rim towards the unreacted core as shown in Fig. 3.25. The resulting elastic modulus is increasing as approaching towards the compact unreacted core. The outward particle rim has a stiffness corresponding to the N-A-S-H gel in the reacted matrix ($\approx$ 17-18 GPa) whereas the hard particle core is bounded by a zone with approximately doubled stiffness. This finding led to the conclusion that indentation hits all four segmented phases.
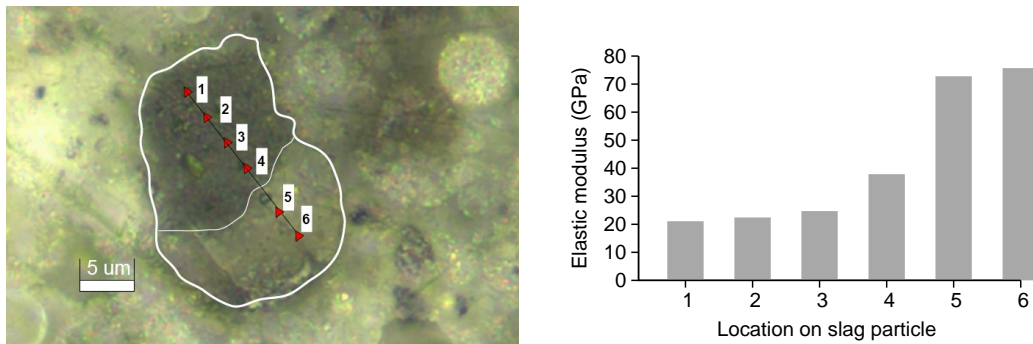
Figure 3.25: Partly-activated slag particle in the heat-cured AAFA sample with marked locations of indents (left) and measured moduli (right).

ESEM and nanoindentation of ambient-cured AAFA

Fig. 3.26 shows a typical morphology for ambient-cured AAFA. The comparison with heat-cured AAFA in Fig. 3.22 shows more capillary pores and darker N-A-S-H gel. This supports the ongoing slow process of N-A-S-H gel syneresis.

Ambient curing produces more homogeneous AAFA on the scale of hundreds of micrometers. In this particular case, three grids from different locations give mutually comparable results, Fig. 3.27.
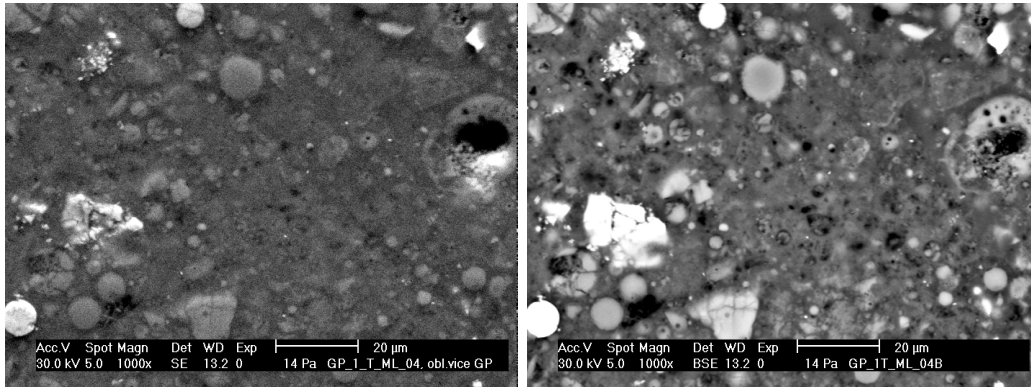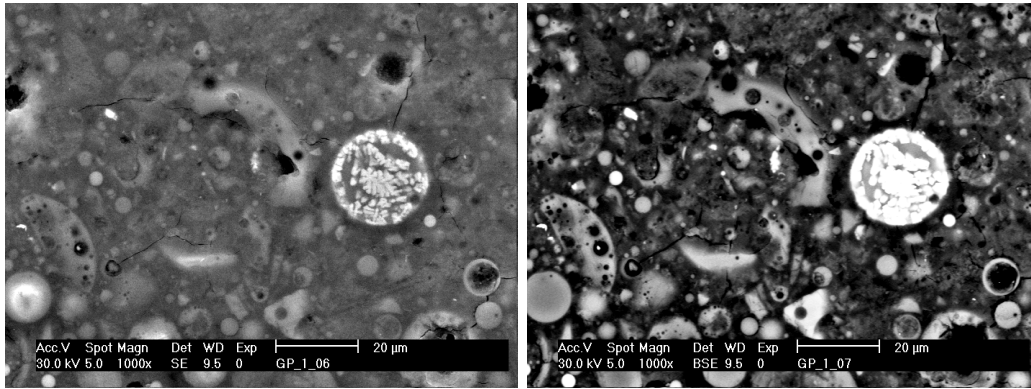
Figure 3.26: AAFA ambient-cured polished samples in SE (left) and BSE (right). BSE image shows white iron and/or iron oxides bullets (intact), and compact Si-Al glass. The spotted light grey particles are partly alkali-activated Si-Al-Na-K fly ash. The original slag particles are dissolved and transformed to dark grey compact matter of N-A-S-H gel. The black spots are capillary pores.
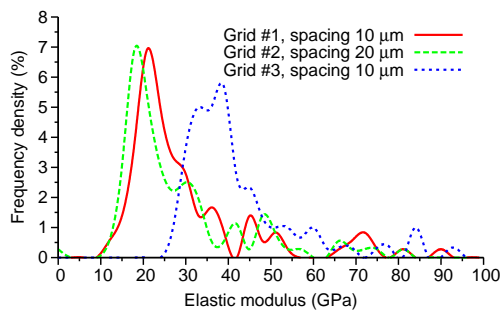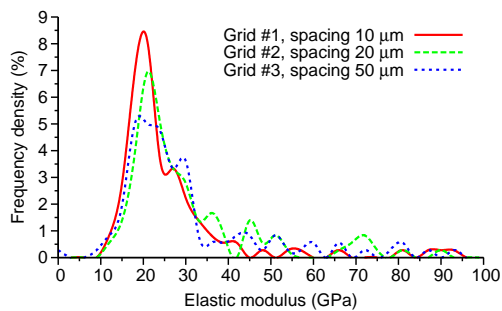

Figure 3.27: Histogram of elastic moduli for three different indentation grids on an ambient-cured AAFA sample.
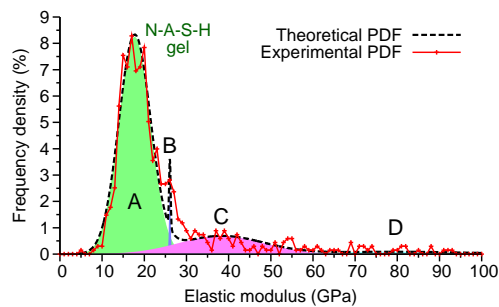
Figure 3.28: Overall experimental and theoretical probability density functions with segmented four phases in ambient-cured AAFA samples.

When compared to heat-cured AAFA, ambient-cured specimens have a much smaller peak associated with partly-activated slag. Such a result points to a better activation under low temperatures. Also, the third and fourth peaks of nonactivated particles are smaller (Fig. 3.28).

ESEM and nanoindentation of heat-cured AAMK

The microstructure of heat-cured metakaolin is very homogeneous (Fig. 3.29). The reason lies in a very monotonous chemical and mineralogical composition of a metakaoline precursor. The dissolving process of the metakaoline matrix is homogeneous and the majority of metakaolin reacts under a strong alkaline activator [58].
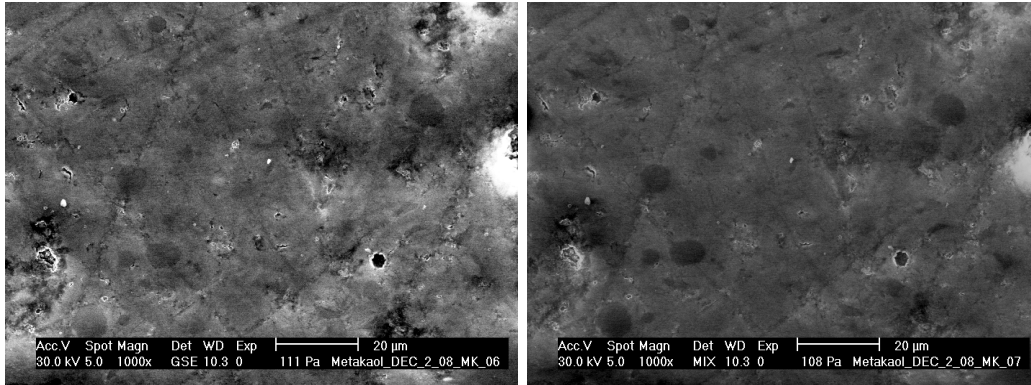
Figure 3.29: AAMK heat-cured polished samples in SE (left) and BSE (right). A few microcracks and pores are distinguishable.

Nanoindentation was again performed as a series of five grids of 100 indents each with mutual distances of $10 - 20$ μm (Fig. 3.30). It follows that, from the micromechanical perspective, activated metakaolin is homogeneous, i.e. raw nonactivated metakaolin is embedded in N-A-S-H gel under the resolution of indentation (≈ 1 μm). Raw metakaolin is present in the quantity of less than 11.2 % by mass. This statement is based on the HCl attacked samples with a weaker 12 M NaOH activator [58].

Statistical deconvolution testifies that N-A-S-H gel is the only dominant phase. The mean value (17.72 GPa) well corresponds to the N-A-S-H gel from heat- and ambient-cured AAFA samples.

Summarized result for AAFA and AAMK samples and comparison with similar materials

Tab. 3.7 summarizes the results from nanoindentation deconvoluted into distinct phases and showing their intrinsic E moduli and frequencies of occurrence. As obvious, N-A-S-H gel was identified with a very similar intrinsic modulus ($\approx 17 - 18$ GPa) regardless of the precursor material. It is worthy to mention that the elastic modulus of N-A-S-H gel is similar to low-density C-S-H gel formed in cement paste (17.8 ± 4.2 GPa, [10]). Compos-
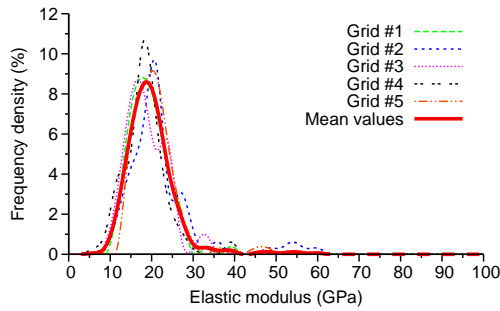
Figure 3.30: Histogram of elastic moduli for five different indentation grids on a heat-cured AAMK sample.
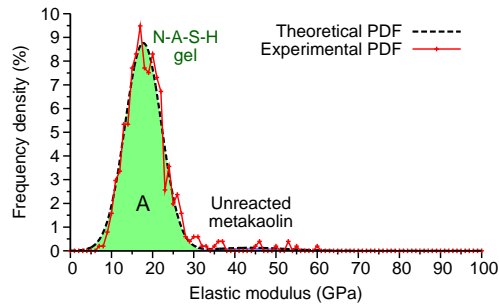
Figure 3.31: Overall experimental and theoretical probability density functions with a segmented dominant N-A-S-H gel phase and unreacted metakaolin in an AAMK sample.

ite materials such as concrete will yield very similar elasticity when cement binder is replaced with AAFA or AAMK. Another material, fused silica, has a typical modulus $72 \pm 2$ GPa and this value roughly corresponds to compact glass found in fly ash. Mullite (aluminosilicate mineral consisting of 72 % Al_2O_3 and 28 % SiO_2), that is partly present in the raw AAFA material, has $E = 223.8 \pm 4.65$ GPa, [59]. Such a high value of the E modulus has never been observed in measurements, either on AAFA or AAMK samples. From nanoindentation virtually no values higher than ≈ 100 GPa were obtained. The reason lies in compliant surrounding matrix which does not allow measuring the intrinsic properties of such hard particles. True intrinsic values obtained by nanoindentation can be achieved if the stiffness contrast between matrix and inclusion is less than five [26].

The indispensable nanoindentation role of assessing intrinsic elastic properties is again demonstrated in Fig. 3.32 from a chemical perspective. The histograms in Fig. 3.32 were obtained by the EDX line analyses, performed on all three activated materials, in the amount 2000 points each. The heat-cured AAMK could be deconvoluted into metakaolin remnants and N-A-S-H gel with Si/Al mean mass ratio 2.16. While alkali-activated materials exhibit very similar Si/Al distribution in Fig. 3.32, the oxide arrangement leads to tremendously different elastic behavior as already demonstrated in Figs. 3.24, 3.28, and 3.31.

Table 3.7: Elastic moduli (GPa) of individual material phases in heat- and ambient-cured AAFA and heat-cured AAMK. The values in parentheses denote frequency.

Phase / precursor and curing	AAFA	
	Heat-cured	Ambient-cured
A. N-A-S-H gel	17.03 ± 3.48 (50.7 %)	17.72 ± 3.75 (77.5 %)
B. Partly-activated slag	29.95 ± 3.66 (26.6 %)	26.06 ± 0.18 (1.1 %)
C. Nonactivated slag	46.90 ± 7.76 (17.6 %)	38.27 ± 10.13 (17.5 %)
D. Nonactivated compact glass	79.15 ± 14.34 (5.1 %)	79.65 ± 16.99 (3.9 %)
Unreacted metakaolin		43.91 ± 8.69 (2.8 %)

Phase / precursor and curing	AAMK
	Heat-cured
A. N-A-S-H gel	17.72 ± 4.43 (97.2 %)
B. Partly-activated slag	-
C. Nonactivated slag	-
D. Nonactivated compact glass	-
Unreacted metakaolin	43.91 ± 8.69 (2.8 %)
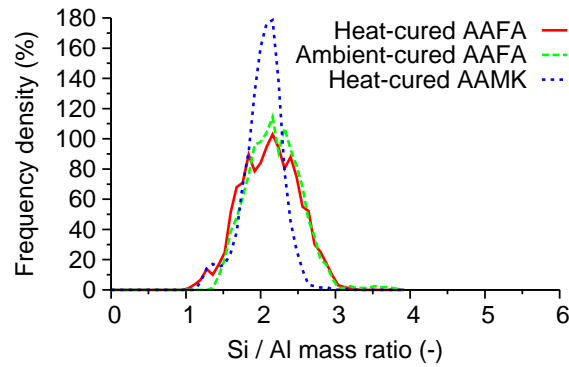
Figure 3.32: Histograms of EDX line analyses demonstrating similar Si/Al distribution in studied three activated materials.

3.4.5 Conclusions

The extensive nanoindentation testing and ESEM analysis of alkali-activated fly ash and metakaolin samples led to the conclusions:

1. The intrinsic E modulus of the main reaction product, the N-A-S-H gel, lies in the range of $17 - 18$ GPa and seems to be independent of the precursor material (fly-ash or metakaolin) and the temperature curing regime (ambient or heat cured) for a given mixture composition. Such

a modulus is very close to a typical value of low-density C-S-H gel, 17.8 GPa, found in cement paste [10]. From the elastic perspective, potential coexistence of C-S-H and N-A-S-H gels is excellent [53].

2. Further deconvolution of indentation histograms identified other elastically distinct phases. Based on thorough argumentation and SEM images, other three morphologically distinct phases were found in AAFA and one in AAMK. The same finding was found on the indenting slag-like activated porous particle.

3. Statistical EDX line analysis provided no evident correlation between chemical composition and the E modulus. Found mean Si/Al mass ratio of N-A-S-H gel is 2.16, corresponding exactly to the value for mature N-A-S-H gel in the form of probably zeolite crystals [48].

4. The slow process of ambient-curing produces a more homogeneous microstructure where no heterogeneity appears on the scale above $10 \times 50 \approx 500$ μm as evident from Fig. 3.27. As opposed, three indentation grids of heat-cured AAFA in Fig. 3.23 show the significant heterogeneity occuring above the scale $10 \times 10 \approx 100$ μm. This emphasizes the ion transport and equilibration of the oligomer concentration during the activation process.

5. Although the study covered typical and mature alkali-activated materials, it is not meant to be exhaustive. Several issues and their effect on elasticity remained open, especially the composition of the mixture and the activator, early age, aging, or ongoing N-A-S-H syneresis.

6. Understanding intrinsic constituent properties in a complex material allows addressing and modeling distinct mechanisms on multiscales in terms of material evolution, performance, optimization and durability. In the history, upscaling of elasticity [4, 60], viscoelasticity [7], or shrinkage [61] proved to be a simple, yet powerful method of conjunction between micromechanics and material engineering.

Chapter 4

Measurement of inelastic properties of cement paste

The most common interpretation of nanoindentation results (the P-h curve, Fig. 1.2) lies in using only unloading portion of the diagram from which elastic properties are evaluated. However, for time-dependent or viscous materials other interpretations are useful. Special role in this is played by the holding period in which loading force is kept constant. At this stage, the viscous character, i.e. creep, is demonstrated by the increase of penetration depth (Fig. 4.1). This period can be used for finding of short-time creep characteristics by using a suitable viscoelastic model, for instance [62].
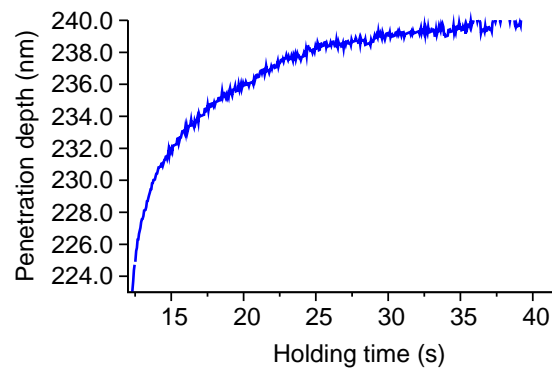
Figure 4.1: Creep of cement paste as observed during holding period (constant force $P = 2$ mN kept for 30 s).

4.1 Indentation size effect versus elastic properties

Size-dependent indentation results of elastic properties are commonly obtained and reported mainly for metals by many researchers, e.g. in [63, 64, 65]. This size effect found in the literature concerns mainly hardness as the only parameter characterizing load-depth diagrams obtained from indentation tests. A similar size effect can be found for elastic modulus in the case of cementitious material as shown e.g. in [1]. Creeping of hydrated phases of this material was found to be the main factor contributing to such interpretations. Ignoring creep and other inelastic phenomena can lead to the spurious size effect on elastic properties and their overestimation.

The effect of the structural size on its strength is widely known and can be understood as the effect of the structural dimension on the nominal strength of the structure when geometrically similar structures are compared. Such sizing is caused mainly by inelastic phenomena that take place in different structural volumes and result in different strengths. In the case of elastic properties, one would expect constant values for a homogeneous isotropic material regardless of the sample size or the size of an indent. A variety of reasons are responsible for a more complicated material behavior and the interpretation of experimental data on the microscale. The most important are summarized below.

1. Specimen preparation. Samples must often undergo a series of mechanical procedures to obtain a flat and smooth surface suitable for indentation. These procedures such as grinding and polishing can produce residual stresses within the surface layers of the material and cause local hardening.

2. Oxidation. Thin oxide layers with mechanical properties different from bulk properties can distort measurements on materials sensitive to oxidation.

3. Indenter friction and adhesion. Some studies also show the effects of friction [66] and adhesion forces [67] between the indenter tip and a sample. Such effects may be significant for soft materials but mainly for small penetration depths (typically less than 100 nm).

4. Surface roughness. Evaluation procedures assume a flat surface with the ideal contact of an indenter. High surface roughness can lead to improper area determination and/or higher local inelastic deformations.

5. Indenter area function. A common source of the indentation size effect is improper estimation of the projected indenter area. Each indenter has to be calibrated due to tip irregularities from its ideal shape. An effective procedure for such calibration was proposed in [14].

6. Development of dislocations. Another reason based on the indentation process can be responsible for the size effect. It is the nucleation of dislocations within the plastic zone under the indentation area [2, 68]. Dislocations can be created in two ways: for statistical reasons and due to the indenter geometry (geometrically necessary dislocations). The presence of dislocations increase the yield strength of the material and this in turn increases the hardness and elastic modulus.

7. Loading time effects. The time of loading (and also unloading) is usually not considered in the evaluation of elastic properties. However, time-dependent material properties can influence the loading diagram from which elastic properties are extracted. Generally speaking, such phenomena associated with loading time are responsible for misinterpretation when using standard tests and standard evaluation procedures [1].

The aforementioned items #1 to #3 are significant for small indents (less than 100 nm) where the depth of penetration affects only the surface layers. For the case of this work, the smallest indentation depth was around 200 nm and the majority of experiments were conducted on this scale where the affected material volume is considerably larger. Surface roughness cannot be fully avoided for cementitious materials since the mechanical preparation of the surface does not allow preparing better surfaces with roughnesses smaller than several tens of nm (as checked by AFM). However, a large number of indents allow statistical evaluation of results, where such local effects are minimized (indicated by standard deviations). The assessment of the indenter area function can be effectively solved using the Oliver - Pharr procedure [14]. The development of dislocations is inevitably present but again it is more significant for small indents and plastic like materials (e.g. metals). Creep effects are very important for soft and time-dependent materials like cement paste. As shown by Němeček [1] loading and holding time is the main factor causing the spurious size effect on the evaluation of elastic properties.

In [1], reduced modulus was evaluated from unloading curves for different load levels of a cyclic loading diagram using either no holding periods at the peak or using 120 s long holding period. It was concluded, that spurious size effect on reduced modulus of hydrated phases of the cement paste appears for the case of no holding period due to the fact that creep occurs during

the unloading (see Fig. 4.2). The creep is manifested by the rounding of the *P-h* curve during unloading as shown in Fig. 4.3 As a remedy, long holding periods that suppress this effects need to be applied for proper estimation of the elastic properties from unloading portions of the *P-h* curve as employed throughout this thesis.
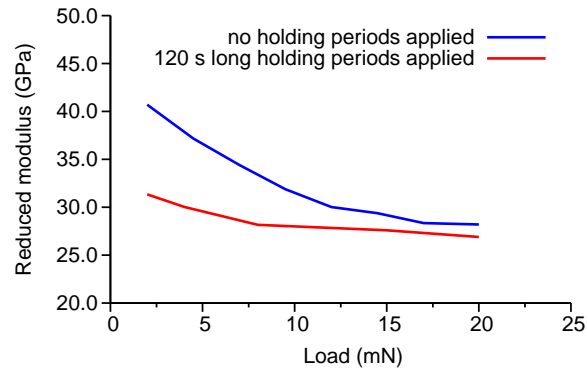
Figure 4.2: Spurious size effect on reduced modulus of hydrated cement (from Němeček [1]).
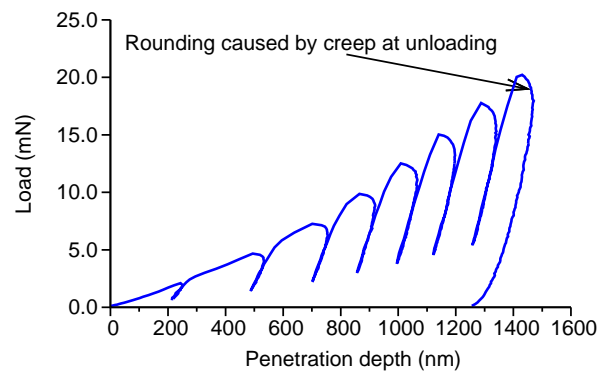
Figure 4.3: Cyclic loading to increasing load levels on cement paste and effect of creep during unloading (from Němeček [1]).

4.2 Quantification of indentation creep

4.2.1 Indentation creep according to ISO14577-1

The creep that occurs during holding period is often characterized by the parameter described in ISO standards [69] that is called indentation creep:

$$C_{(P,t_1,t_2)} = \frac{h_2 - h_1}{h_1} \times 100(\%) \tag{4.1}$$

which is computed from the relative difference between penetration depths h_1 and h_2 during holding period and is dependent on the constant load level P which was reached at time t_1 and creep duration t_2. Although it seems that this parameter could be used for comparison of creeping materials it can be misleading as illustrated in Fig. 4.4 because it can give the same result for differently creeping materials. Therefore, some other characteristics that take into account the whole character of the creeping curve are appropriate in this case.
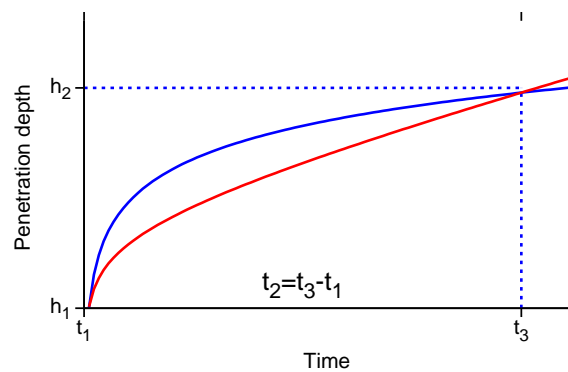
Figure 4.4: Indentation creep for differently creeping materials giving the same ISO14577-1 creep.

4.2.2 Characterization of creep using linear viscoelastic models

As mentioned in Section 3.3 time-dependent, i.e. viscous behavior can be attributed purely to hydrated phases in cement paste. In order to describe this, suitable viscoelastic model can be employed. For a viscoelastic material, two basic elements are used to describe the elastic and viscous parts of the deformation: the spring and the dashpot. Each element is assigned by

a material constant, i.e. elastic modulus E_i in case of a spring and viscosity η_i in case of a dashpot. Two to infinite number of the elements can create a deformable chain in which elements are connected in serial or parallel way. For a short-time creep, models with limited number of parameters are useful because analytical solutions [70] can be easily obtained for these chains Fig. 4.5.
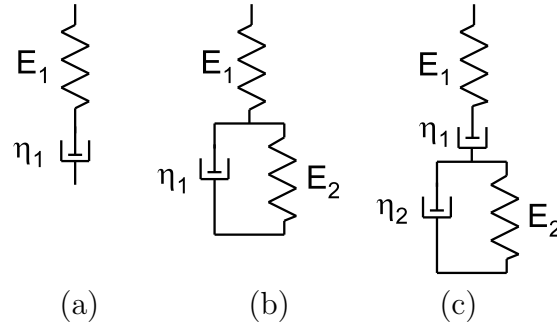
Figure 4.5: Viscoelastic models: (a) Maxwell, (b) Kelvin-Voigt and (c) Kelvin-Voigt-Maxwell or Burgers chains.

For the two-element model (so called Maxwell unit, Fig. 4.5 a) the total uniaxial strain rate $\dot{\varepsilon}$ can be expressed as:

$$\dot{\varepsilon} = \frac{\dot{\sigma}}{E_1} + \frac{\sigma}{\eta_1} \tag{4.2}$$

which can be solved by direct integration. For a constant stress $\sigma = \sigma_0$ applied at time $t = t_0$ one gets:

$$\varepsilon = \frac{\sigma_0}{E_1} + \frac{\sigma_0}{\eta_1}t \tag{4.3}$$

In case of a conical indenter (with the tip halfangle α) and by applying constant load P_0 the surface deflection takes the form [71]:

$$h^2(t) = \frac{\pi}{2}P_0 cot\alpha \left(\frac{1}{E_1} + \frac{1}{\eta_1}t\right) \tag{4.4}$$

For the three-element model (Kelvin-Voigt unit, Fig. 4.5 b) the compatibility condition reads:

$$E_1 E_2 \varepsilon + E_1 \eta_1 \varepsilon = (E_1 + E_2)\sigma + \eta_1 \dot{\sigma} \tag{4.5}$$

which can be again readily solved by direct integration with the solution for constant stress ($\sigma = \sigma_0$ applied at time $t = t_0$):

$$\varepsilon = \sigma_0 \left[\frac{1}{E_1} + \frac{1}{E_2} \left(1 - e^{-t\frac{E_2}{\eta_1}} \right) \right] \tag{4.6}$$

and for a conical indenter:

$$h^2(t) = \frac{\pi}{2} P_0 cot\alpha \left(\frac{1}{E_1} + \frac{1}{E_2} \left(1 - e^{-t\frac{E_2}{\eta_1}} \right) \right) \tag{4.7}$$

For the four-element model (Kelvin-Voigt-Maxwell or Burgers chain, Fig. 4.5 c) one gets:

$$h^2(t) = \frac{\pi}{2} P_0 cot\alpha \left(\frac{1}{E_1} + \frac{1}{E_2} \left(1 - e^{-t\frac{E_2}{\eta_2}} \right) + \frac{1}{\eta_1} t \right) \tag{4.8}$$

Recent work of Vandamme and Ulm [62] assumes that the indentation response of the hydrated cement paste is dominated by the linear viscoelastic behavior. In this work, the best results were obtained using the combined Kelvin-Voigt-Maxwell chain with four parameters applied to deviatoric stress components (Fig. 4.6).
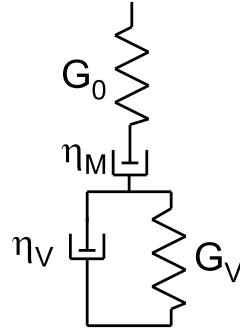
Figure 4.6: Deviator creep model based on Kelvin-Voigt-Maxwell chain.

The solution presented in [62] uses the framework of linear viscoelastic indentation analysis based on the method of functional equations developed by Lee and Radok [72]. Vandamme et al. [62] derived closed form solutions for different linear viscoelastic models for relevant indentation load histories. In continuum mechanics, the viscoelastic constitutive relations are often expressed by using creep or relaxation functions, $\mathbf{C}$ or $\mathbf{R}$:

$$\boldsymbol{\varepsilon} = \int_0^t \mathbf{C}(t - \tau) : \frac{d}{d\tau} \boldsymbol{\sigma}(\tau) d\tau. \tag{4.9}$$

$$\boldsymbol{\sigma} = \int_0^t \mathbf{R}(t - \tau) : \frac{d}{d\tau} \boldsymbol{\varepsilon}(\tau) d\tau \tag{4.10}$$

For the case of combined Kelvin-Voigt-Maxwell chain applied to deviator creep (Fig. 4.6) of the linear isotropic viscoelastic material, the creep function takes the form:

$$C^d(t) = \frac{1}{G_0} + \frac{1}{G_V}\left(1 - e^{-t\frac{G_V}{\eta_V}}\right) + \frac{1}{\eta_M}t \qquad (4.11)$$

An analytical solutions are then provided for conical indentation and application of e.g. a step load or trapezoidal loading history that is commonly used [62]. The analytical solution is, however, restricted to monotonically increasing loads or strictly speaking increasing contact area which holds for loading and holding periods and may hold for the initial part of unloading. But, the attractivity of the solution inheres in the direct application of it to the fitting of viscoelastic material parameters from holding periods of the nanoindentation *P-h* curve as will be demonstrated later.

4.2.3 Identification of viscoelastic parameters of cement paste

The linear viscoelastic framework described in previous section was applied for the characterization of inelastic parameters of cement paste. The same specimens and the same *P-h* data as in Section 3.3 were used for this study. First, the viscoelastic parameters were identified from the 30 s long holding period (Fig. 4.7). The reduced modulus or the Young's modulus E_0, respectively derived from the unloading curve by Oliver-Pharr method were used to estimate the first shear modulus G_0 in the chain of Fig. 4.6:

$$G_0 = \frac{E_0}{2(1+\nu)} \qquad (4.12)$$

Then, other three parameters were fitted by the nonlinear least square method from the holding period of the creep curve as shown in Fig. 4.8. For the sake of comparison, the same previously fitted parameters were used for computing of the loading period as well. Good agreement between the experimental and computed curve was achieved as depicted in Fig. 4.9. Unloading was not computed since the analytical solution is not valid for the decreasing contact area. In this study, results only for well hydrated phases, i.e. C-S-H and CH were taken into account and average parameters were examined. The distinction from other phases was based on reduced modulus. Only indents having the reduced modulus in the range $20 - 35$ GPa were considered. Viscoelastic parameters fitted for all the hydrated phases are summarized in Tab. 4.1. It can be seen that a relatively large scatter appears in the parameters but based on several trial&error tests it was found that the sensitivity of

the *P-h* response on the exact value of the parameters (in terms of Fig. 4.9) is not so high.
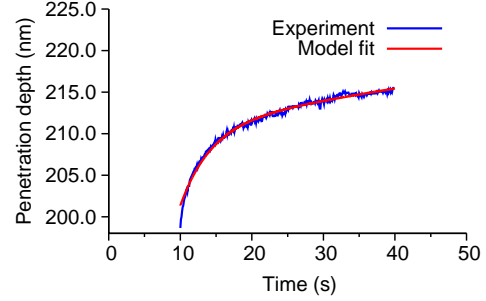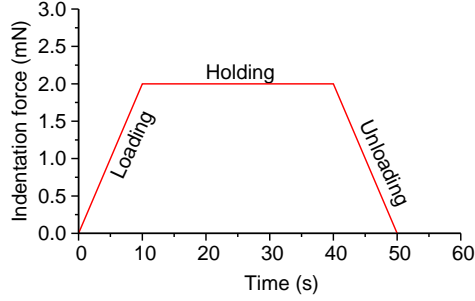
Figure 4.7: Prescribed loading diagram in indentation experiments.

Figure 4.8: Fitting of viscoelastic parameters from the holding period.
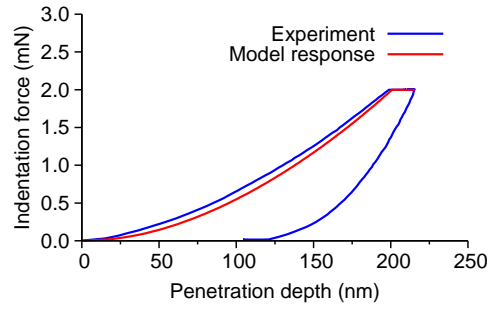
Figure 4.9: Comparison of experiment and model response during loading.

Table 4.1: Viscoelastic parameters of hydrated phases of cement paste fitted from holding periods

Parameter	E_r (GPa)	η_M (GPa·s)	η_V (GPa·s)	G_V (GPa)
Average	26.46 ± 3.55	5303.6 ± 1253.7	21.1 ± 5.6	3.26 ± 0.52
Min	20.57	9423.8	35.3	4.40
Max	34.76	3542.1	11.6	2.13

4.2.4 Concluding remarks

It was shown in previous section that linear visvoelastic model can give a good estimate of the short-time creep characteristics in terms of creep (or relaxation) function rather than using simplified scalar parameters (e.g. ISO creep). The limited number of viscoelastic units in the chain is sufficient for the description of the indentation loading process, however, for a long time predictions some more general approaches (e.g. generalized Kelvin-Maxvell chains [70]) could be appropriate.

Chapter 5

Modeling of nanoindentation process

The model description of the nanoindentation process and appropriate continuum constitutive models will be discussed in this chapter. Combining nanoindentation with a modeling and especially finite element analysis may further enhance this experimental technique and address many of the phenomena associated with the process like size-effect, creep, plastic deformations etc. On one hand, results of numerical simulations can provide a valuable feedback to experiments by helping to select appropriate loading histories and indentation depths (e. g. with regard to the topology of the material microstructure). On the other hand, by using more advanced nonlinear material models to fit the response obtained from a nanoindentation test, it can become possible to retrieve characteristics describing plastic and viscous behavior of the material phases. This chapter focuses on testing the ability of various constitutive relations to qualitatively reproduce the response of a hydrated phase of hardened cement paste measured in a cyclic nanoindentation experiment.

5.1 Experimental part

White cement paste samples (CEM-I 52,5 White, Holcim, SK) mixed in water to cement ratio w/c=0.5 were prepared and stored in water for 28 days. Before testing, ≈ 4 mm thick slice from the bulk material was cut and polished on coarse to very fine emery papers to achieve very smooth and flat surface. Specimens were washed in ultrasonic bath to remove the dust. The resultant surface had the roughness about several tens of nm as checked by AFM. Indentation was performed with Nanotest (Micro Materials, UK) nanoindenter equipped with Berkovich indenter. Cyclic loading history with increasing

peak loads was prescribed as shown in Fig. 5.1. Proportional loading with a constant strain rate $\dot{\varepsilon} = 0.15$ s $^{-1}$ was applied followed by 120 s long holding segment and linear unloading 0.3 mN/s to 20 % of the peak load. After nanoindentation, imprints were identified in ESEM and separated to group belonging to hydrated phases. A cluster of *P-h* curves was obtained for these hydrated phases. From these curves a typical one was selected for the forthcoming numerical reproduction (Fig. 5.2).
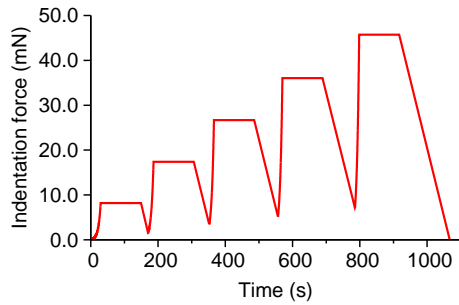
Figure 5.1: Prescribed loading diagram in five-cycle indentation experiments.
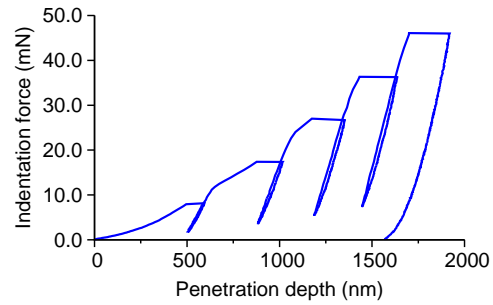
Figure 5.2: Example of cyclic load-penetration curve obtained for hydrated cement paste by nanoindentation.

5.2 Finite element model

In order to find a constitutive model that would be able to represent the experimentally obtained behavior of the hydrated phase, a series of numerical simulations of the nanoindentation experiment by finite element (FE) model was carried out. Nanoindentation was modeled as a contact problem of a deformable body (specimen) which was pushed against a rigid conical indenter. The geometry was simplified in FE model by assuming axial symmetry of both the indenter and the material specimen. The height of the modeled domain was equal to that of the real specimen ($\approx$ 4 mm), while the diameter was reduced to one half ($\approx$ 15 mm) which is still much larger than the zone affected by any indent. The FE mesh consisted of 1800 isoparametric four-node elements and it was significantly refined in the proximity of the indent (Fig. 5.3). The indenter was modeled as perfectly rigid and its variable contact with the specimen was identified and imposed in each loading step. Large deformations and large displacements were taken into account. Constitutive relations discussed hereafter were applied to the Cauchy stress and

logarithmic strain. The analyses were carried out with the general-purpose FE program ADINA. Several constitutive relations were tested in this work.

Figure 5.3: Axially symmetric FE mesh of the indenter–specimen contact problem.

5.2.1 Linear viscoelastic model

As a first approximation, linear viscoelastic model with deviatoric creep described in Section 4.2.2 was used. The Young's modulus E_0 was estimated from the first unloading b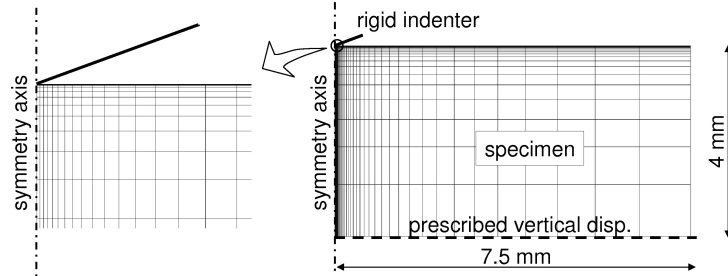ranch by the standard Oliver and Pharr method [14], and corresponding shear modulus G_0 (Eq. (4.12)) assuming that Poisson's ratio is 0.2. Then the viscoelastic parameters were identified by fitting of the experimental creep response measured during the first holding period. The applicability of this model was found to be limited only to loading and holding period (from which the model parameters are fitted whereas the unloading branch as well as the hysteresis of the subsequent cycles was not captured correctly as shown in Figs 5.4 and 5.5. The reason for that lies probably in the formulation of the viscoelastic model itself. It does not behave elastically even on the unloading branch because the dashpot elements in the chain (Fig. 4.6) act whenever the strain rate is nonzero.

5.2.2 Nonlinear viscoelastic model

As an enhancement, the nonlinear viscoelastic model based on the creep potential formulation was used. The stress–strain relationship involved the decomposition of the strain tensor into elastic and viscous parts:

$$\boldsymbol{\sigma} = \mathbf{S} : (\boldsymbol{\varepsilon} - \boldsymbol{\varepsilon}^c) \tag{5.1}$$

where $\mathbf{S}$ is the elastic stiffness tensor, $\boldsymbol{\sigma}$ and $\boldsymbol{\varepsilon}$ stand for the stress and strain tensors, respectively and $\boldsymbol{\varepsilon}^c$ is the creep strain tensor. The evolution of the creep strain was governed by a creep flow rule:
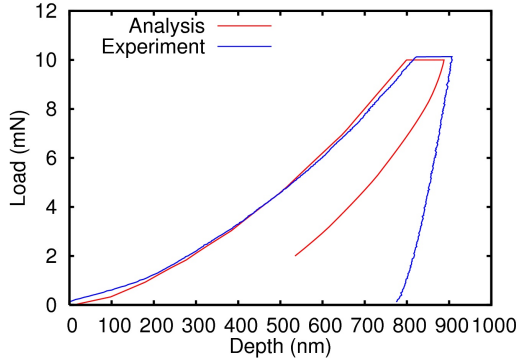
Figure 5.4: Performance of linear viscoelastic model on one cycle test.
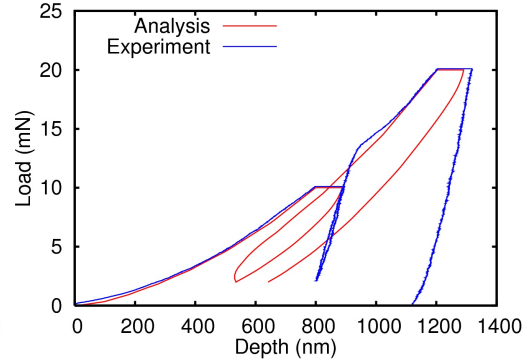
Figure 5.5: Performance of linear viscoelastic model on two cycles test.

$$\dot{\boldsymbol{\varepsilon}}^c = \gamma \frac{\partial J_2}{\partial \boldsymbol{\sigma}} \qquad (5.2)$$

where a dot symbol above indicates time rate and J_2 is the creep potential expressed by the second invariant of the deviatoric stress tensor. Scalar γ depends on the current value of equivalent stress:

$$\bar{\sigma} = \sqrt{3J_2} \qquad (5.3)$$

and the equivalent creep strain, which is expressed by the power creep law:

$$\bar{\varepsilon}^c = a_0 \bar{\sigma}^{a_1} t^{a_2} \qquad (5.4)$$

in which a_0, a_1, a_2 are material constants and t stands for time. A parametric study was carried out to find the model parameters such that the results of the FE simulation provided the best fit of the first cycle of loading-holding-unloading. Fig. 5.6 shows that this goal was satisfactorily met. However, the subsequent loading cycles showed a significant deviation from the experiment. In particular, the subsequent loading branches lacked the typical kink that occurred shortly after exceeding the maximum load from the previous cycle. This resulted in the total displacement at the end of the analysis lower than that obtained from the experiment. On the other hand, the behavior during unloading was matched fairly well.

5.2.3 Combined nonlinear viscoelastic and plastic model

As a next step, the nonlinear viscoelastic model was enhanced by a plastic element, assuming that the kink during loading could be attributed to plastic yielding. The employed constitutive model utilized the decomposition of the strain tensor:

$$\varepsilon = \varepsilon^E + \varepsilon^C + \varepsilon^P \tag{5.5}$$

where ε^P stands for plastic strain tensor. In contrary to creep strains, plastic strains develop only upon satisfaction of the applied von Mises yield condition:

$$J_2 = \frac{1}{3}\sigma_Y = 0 \tag{5.6}$$

in which σ_Y is a material parameter (uniaxial yield strength). The evolution of plastic strain then follows the associated flow rule and perfect plasticity. Therefore, the present model involves two nonlinear phenomena: creep and plasticity. These phenomena cannot be simply separated in the force-controlled nanoindentation test, since even under a constant force (during the holding period) the material creeps, which results in a variable contact area with the indenter and therefore a variable stress field under the indenter. Consequently, the parameters were determined by a trial and error approach, which probably did not provide the optimum values. Nevertheless, this deficiency does not prevent one from examining some general features of the model. Fig. 5.7 shows that the combined nonlinear viscoelastic and plastic model qualitatively reproduced all the characteristic features of the measured nanoindentation curve. As opposed to the previous models, the present one did not exaggerate the hysteresis during unloading–reloading and properly captured the kink during the subsequent loading. However, proper identification of the combined model is a difficult task and is beyond the scope of this work.

The FE model also gives information on deformations and stress field under the indenter probe as shown in Figs 5.8 and 5.9 where the effective plastic and creep strains are plotted after the second loading cycle (Fig. 5.7 (a)). Figs 5.10 and 5.11 show the effective plastic and creep strains after the full load removal (Fig. 5.7 (b)). It can be seen that a significant plastic as well as creep deformations remain accumulated in the material under the indenter even after full unloading.

5.2.4 Concluding remarks

The presented numerical work concerned on the evaluation of nanoindentation process measured on hydrated phases of cement pastes. The comparison
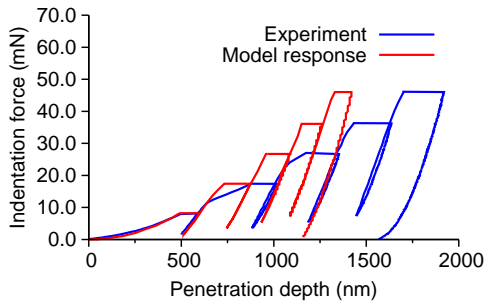
Figure 5.6: Performance of nonlinear viscoelastic model.
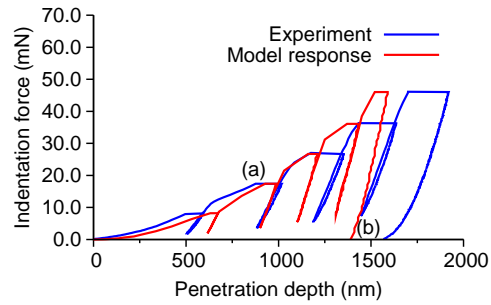
Figure 5.7: Performance of combined nonlinear viscoelastic plastic model.
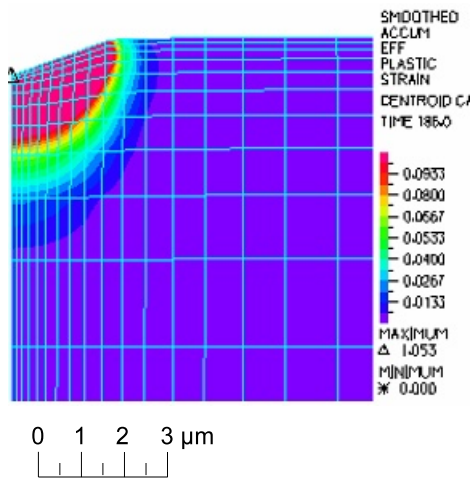
Figure 5.8: Effective plastic strain under the indenter after the second cycle (see Fig. 5.7 (a)).
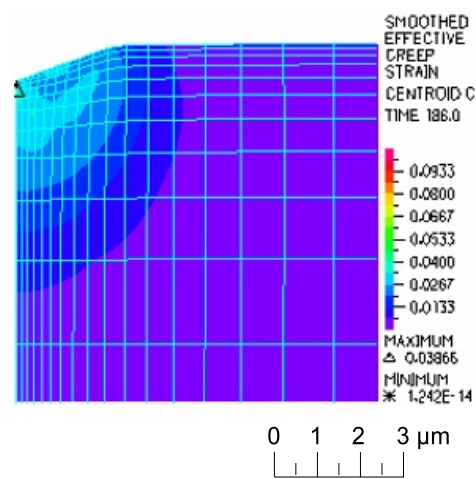
Figure 5.9: Effective creep strain under the indenter after the second cycle (see Fig. 5.7 (a)).

of several constitutive models was shown. A simple viscoelastic solution (Vandamme and Ulm [62]) can capture the loading and holding periods of the *P-h* curve for one cycle experiment. However, using of the same material parameters does not lead to satisfactory results for the case of cyclic loading. Thus, a more general FE model was proposed. The FE analyses showed that in description of the micromechanical behavior of cement paste, both time-independent plastic strains and time-dependent creep stains appear to play an important role. The model that combined nonlinear viscoelastic and plastic elements provided the best qualitative match to the experimentally measured response also for complex loading histories like cyclic loading. However,
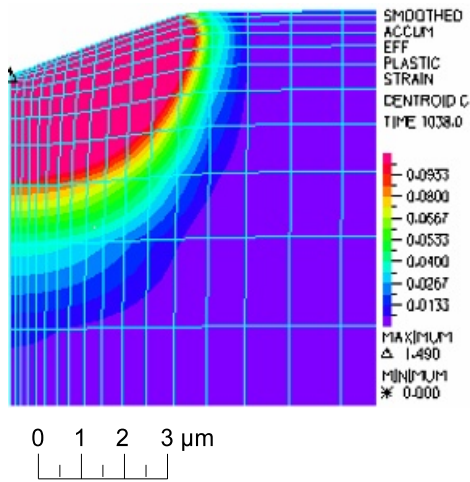
Figure 5.10: Effective plastic strain under the indenter after the load removal (see Fig. 5.7 (b)).
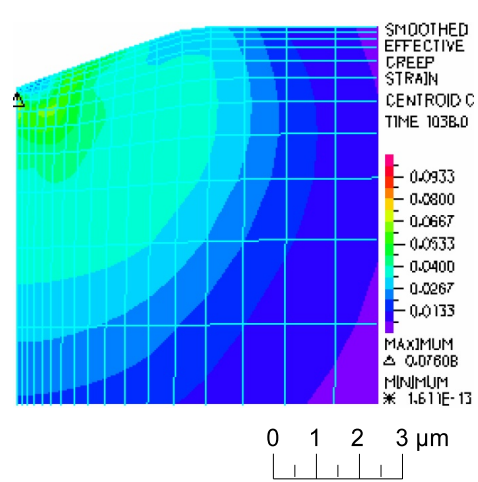
Figure 5.11: Effective creep strain under the indenter after the load removal (see Fig. 5.7 (b)).

parameters of the qualitatively most suitable elastic-plastic-creep model are difficult to obtain. Simple trial and error procedure does not lead to satisfactory qualitative results and rigorous fitting faces significant obstacles that are caused by the impossibility to distinguish between plastic and viscous deformation during loading. Rigorous identification of the model parameters and quantitatively equivalent simulations remain as a future perspective of the research.

Chapter 6

Summary

It was shown on several examples of structural materials that nanoindentation is a powerful technique that plays an indispensable role in the micromechanical testing of heterogeneous solids. Extensive measurements on cement pastes and alkali-activated fly ash (AAFA) was presented in this thesis with the primary interest in elastic and inelastic properties of individual material phases. Intrinsic elastic properties of C-S-H gels and Portlandite, were determined by means of massive grid indentation with the aid of subsequent statistical deconvolution. An efficient deconvolution procedure leading to unambiguous results has been proposed in this work. Some of the material phases, like high-density C-S-H or clinker were detected by pointed nanoindentation. Pioneer measurements on AAFA were performed and mutual similarities with cementitious materials have been disclosed. AAFA appears to be a good candidate for a partial replacement of ordinary Portland cement in specific structural applications. Generally, obtained results were found to be in good agreement with available literature results and good correlation with supplementary analyses, e.g. ESEM, EDX and porosimetry.

Simple analytical homogenization strategies were successfully applied to the lowest levels of cementitious composite in order to obtain effective elastic properties of cement paste. Inelastic properties of hydrated cement paste were studied in conjunction with viscoelastic models. Viscoelastic parameters were determined from the holding period of a standard one-cycle test. Such approach was found to be simple and efficient for a short-term creep characterization. However, limited usage of such parameters was discovered during modeling of indentation process. Several approaches employing nonlinear viscoelasticity and plasticity were studied in order to find qualitatively most suitable model for description of hydrated cement paste behavior. The FE analyses showed that both time-independent plastic strains and time-dependent creep strains appear to play an important role in this nanoinden-

tation process. The model that combined nonlinear viscoelastic and plastic elements provided the best qualitative match to the experimentally measured response also for complex loading histories like cyclic loading. However, identification of the model parameters is not straightforward and remains as a future goal.

Bibliography

[1] J. Němeček, Creep effects in nanoindentation of hydrated phases of cement pastes, Materials Characterization 60 (2009) 1028–1034.

[2] A. C. Fischer-Cripps, Nanoindentation, Springer, 2002.

[3] P. Tennis, H. Jennings, A model for two types of calcium silicate hydrate in the microstructure of Portland cement pastes, Cem. Concr. Res. 30 (2000) 855–863.

[4] O. Bernard, F.-J. Ulm, E. Lemarchand, A multiscale micromechanics-hydration model for the early-age elastic properties of cement-based materials, Cem. Concr. Res. 33 (9) (2003) 1293–1309.

[5] J. Nadeau, A multiscale model for effective moduli of concrete incorporating ITZ water-cement ratio gradients, aggregate size distributions, and entrapped voids, Cem. Concr. Res. 33 (2003) 103–113.

[6] V. Šmilauer, Z. Bittnar, Micromechanical Multiscale Simulation of Elastic Properties of Hydrating Concrete, in: Proc. of the Eight International Conference on Computational Structures Technology, 2006, pp. 153–154.

[7] C. Pichler, R. Lackner, A multiscale creep model as basis for simulation of early-age concrete behavior, Computers and Concrete 5 (4) (2008) 295 – 328.

[8] A. Zaoui, Continuum Micromechanics: Survey, Journal of Engineering Mechanics 128 (8) (2002) 808–816.

[9] K. Velez, S. Maximilien, D. Damidot, G. Fantozzi, F. Sorrentino, Determination by nanoindentation of elastic modulus and hardness of pure constituents of Portland cement clinker, Cem. Concr. Res. 31 (2001) 555–561.

[10] G. Constantinides, F.-J. Ulm, The effect of two types of C-S-H on the elasticity of cement-based materials: results from nanoindentation and micromechanical modeling, Cem. Concr. Res. 34 (1) (2004) 67–80.

[11] H. Hertz, On the contact of elastic solids, J. Reine Angew. Math. 92 (1881) 156–171, translated and reprinted in English in *Hertz's Miscellaneous Papers*, Macmillan & Co, London, 1896, Ch. 6.

[12] J. Boussinesq, Application des potentiels a l'etude de l'equilibre et du mouvement des solides elastiques, Paris.

[13] I. Sneddon, The relation between load and penetration in the axisymmetric Boussinesq problem for a punch of arbitrary profile, International Journal of Engineering Science 3 (1965) 47–57.

[14] W. Oliver, G. Pharr, An improved technique for determining hardness and elastic modulus using load and displacement sensing indentation experiments, Journal of Material Research 7 (1992) 1564–1583.

[15] R. King, Elastic analysis of some punch problems for a layered medium, Int. J. Solids Struct. 23 (1987) 1657–1664.

[16] F. Lea, Lea's Chemistry of Cement and Concrete, 4th Edition, Elsevier, 2004.

[17] H. Taylor, Cement Chemistry, Academic Press, New York, 1990.

[18] W. Czernin, Cement Chemistry and Physics for Civil Engineers, 2nd Edition, Bauverlag GmbH, Wiesbaden und Berlin, 1980.

[19] E. Garboczi, D. P. Bentz, Computer Modelling of Interfacial Transition Zone: Microstructure and Properties, report 20, RILEM ETC report, Cachan, France (1999).

[20] J. Michel, H. Moulinec, P. Suquet, Effective properties of composite materials with periodic microstructure: a computational approach, Meth-ods. Appl. Mech. Engng. 172 (1999) 109–143.

[21] N. Randall, Mechanical properties of cementitious materials, Application Bulletin 29, CSM Instruments, http://www.csm-instruments.com/ (2009).

[22] G. Constantinides, F.-J. Ulm, The nanogranular nature of C-S-H, Journal of the Mechanics and Physics of Solids 55 (2007) 64–90.

[23] F. M. Borodich, L. M. Keer, C. S. Korach, Analytical study of fundamental nanoindentation test relations for indenters of non-ideal shapes, Nanotechnology 14 (2003) 803808.

[24] R. Hill, Continuum micro-mechanics of elastoplastic polycrystals, J. Mech. Phys. Solids 13 (1965) 89–101.

[25] Z. Hashin, Analysis of composite materials - A survey, Journal of Applied Mechanics - Transactions of the ASME 50 (3) (1983) 481–505.

[26] G. Constantinides, K. R. Chandran, F.-J. Ulm, K. V. Vliet, Grid indentation analysis of composite microstructure and mechanics: Principles and validation, Materials Science and Engineering A (430) (2006) 189–202.

[27] H. Buckle, The Science of Hardness Testing and its Research Applications, American Society for Metals, J.W. Westbrook, H. Conrad (Eds.) (1973) 453–491Metals Park, OH.

[28] K. Durst, M. Goken, H. Vehoff, Finite element study for nanoindentation measurements on two-phase materials, J. Mater. Res. 19 (1) (2004) 85–93.

[29] H. Gao, C. Chiu, J. Lee, Elastic contact versus indentation modeling of multi-layered materials, International Journal of Solids and Structures 29 (20) (1992) 2471–2492.

[30] R. Hill, Theory of mechanical properties of fiber-strengthened materials. - III: Self-consistent model, J. Mech. Phys. Solids 13 (1965) 189–198.

[31] J. Eshelby, The determination of the elastic field of an ellipsoidal inclusion and related problems, in: Proc. Royal Society of London A, 1957, pp. 376 – 396.

[32] T. Mori, K. Tanaka, Average stress in matrix and average elastic energy of materials with misfitting inclusions, Acta Metallurgica 21 (5) (1973) 1605–1609.

[33] E. Hervé, A. Zaoui, N-layered Inclusion-based Micromechanical Modelling, Int. J. Engng Sci. 31 (1993) 1–10.

[34] F. Heukamp, E. Lemarchand, F. Ulm, The effect of interfacial properties on the cohesion of highly filled composite materials, International Journal of Solids and Structures 42 (1) (2005) 287–305.

[35] Z. Hashin, S. Shtrikman, On some variational principles in anisotropic and nonhomogeneous elasticity, J. of the Mechanics and Physics of Solids 10 (1962) 335–342.

[36] J. Zeman, Analysis of composite materials with random microstructure, Ph.D. thesis, CTU Reports, ČVUT Praha (2003).

[37] C. Huet, Application of variational concepts to size effects in elastic heterogeneous bodies, J. Mech. Phys. Solids 38 (1990) 813–841.

[38] E. Garboczi, Finite element and finite difference programs for computing the linear electric and elastic properties of digital images of random materials, Tech. rep., NIST Building and Fire Research Laboratory, Gaithersburg, Maryland (1998).

[39] H. Moulinec, P. Suquet, A fast numerical method for computing the linear and nonlinear mechanical properties of composites, Comptes Rendus de l'Academie des Sciences Serie II 318 (11) (1994) 1417–1423.

[40] Iso 4287:1997 geometrical product specifications (gps) – surface texture: Profile method – terms, definitions and surface texture parameters, Iso 4287:1997 (1997).

[41] H. Jennings, A model for the microstructure of calcium silicate hydrate in cement paste, Cem. Concr. Res. 30 (6) (2000) 101–116.

[42] D. P. Bentz, Quantitative comparison of real and CEMHYD3D model microstructures using correlation functions, Cem. Concr. Res. 36 (2) (2006) 259–263.

[43] K. Scrivener, Backscattered electron imaging of cementitious microstructures: understanding and quantification, Cement and Concrete Composites 26 (8) (2004) 935–945.

[44] N. Randall, M. Vandamme, F. Ulm, Nanoindentation analysis as a two-dimensional tool for mapping the mechanical properties of complex surfaces, Journal of Materials Research 24 (3) (2009) 679–690.

[45] F. Pacheco-Torgal, J. Castro-Gomes, S. Jalali, Alkali-activated binders: A review: Part 1. Historical background, terminology, reaction mechanisms and hydration products, Construction and Building Materials 22 (7) (2008) 1305 – 1314.

[46] P. Duxson, A. Fernández-Jiménez, J. L. Provis, G. C. Lukey, A. Palomo, J. S. J. van Deventer, Geopolymer technology: the current state of the art, Journal of Materials Science 42 (9) (2007) 2917 – 2933.

[47] C. Shi, P. V. Krivenko, D. Roy, Alkali-activated cements and concrete, Taylor & Francis, 2006, .

[48] A. Fernández-Jiménez, A. Palomo, Composition and microstructure of alkali activated fly ash binder: Effect of the activator, Cem. Concr. Res. 35 (2005) 1984–1992.

[49] V. Glukhovsky, Soil Silicates (Gruntosilikaty), Kiev, Budivelnik publisher, USSR, 1959.

[50] J. Davidovits, Synthesis of new high-temperature geo-polymers for reinforced plastics/composites, in: Proceedings of PACTEC'79, Society of Plastic Engineers, 1979, pp. 151–154.

[51] F. Škvára, L. Kopecký, V. Šmilauer, Z. Bittnar, Material and structural characterization of alkali activated low-calcium brown coal fly ash, Journal of Hazardous Materials 168 (2009) 711–720.

[52] I. Beleña, W. Zhu, Nanoindentation Study of Na-Geopolymers Exposed to High Temperatures, in: Z. Bittnar, P. Bartos, J. Zeman, J. Němeček, V. Šmilauer (Eds.), Proceedings of the Nanotechnology in Construction 3, Springer, 2009, pp. 169 – 174.

[53] A. Palomo, A. Fernández-Jiménez, G. Kovalchuk, L. M. Ordoñez, M. C. Naranjo, Opc-fly ash cementitious systems: study of gel binders produced during alkaline hydration, J Mater Sci 42 (9) (2007) 2958 – 2966.

[54] M. L. Granizo, M. T. Blanco-Varela, S. Martínez-Ramírez, Alkali activation of metakaolins: parameters affecting mechanical, structural and microstructural properties, J Mater Sci 42 (9) (2007) 2934–2943.

[55] D. Hardjito, , B. Rangan, Development and properties of low-calcium fly ash-based geopolymer concrete, Research report gc 1, Curtin University of Technology, Perth, Australia, faculty of Engineering (2005).

[56] S. Wallah, B. Rangan, Low-calcium fly ash-based geopolymer concrete: Long term properties, Research Report GC 2, Curtin University of Technology, Perth, Australia (2006).

[57] A. Fernández-Jiménez, A. Palomo, M. Criado, Microstructure development of alkali-activated fly ash cement: a descriptive model, Cem. Concr. Res. 35 (2004) 1204–1209.

[58] M. L. Granizo, S. Alonso, M. T. Blanco-Varela, A. Palomo, Alkaline Activation of Metakaolin: Effect of Calcium Hydroxide in the Products of Reaction, Journal of the American Ceramic Society 85 (1) (2002) 225–231.

[59] S. Nath, A. Dey, A. Mukhopadhyay, B. Basu, Nanoindentation response of novel hydroxyapatite-mullite composites, Materials Science and Engineering A (513-514) (2009) 197–201.

[60] V. Šmilauer, Z. Bittnar, Microstructure-based micromechanical prediction of elastic properties in hydrating cement paste., Cem. Concr. Res. 36 (9) (2006) 1708–1718.

[61] C. Pichler, R. Lackner, H. A. Mang, A multiscale micromechanics model for the autogenous-shrinkage deformation of early-age cement-based materials, Engineering Fracture Mechanics 74 (2007) 34–58.

[62] M. Vandamme, F. Ulm, Viscoelastic solutions for conical indentation, International Journal of Solids and Structures 43 (10) (2006) 3142–3165.

[63] Y. Choi, K. Van Vliet, J. Li, S. Suresh, Size effects on the onset of plastic deformation during nanoindentation of thin films and patterned lines, Journal of Applied Physics 94 (2003) 6050.

[64] A. Elmustafa, D. Stone, Indentation size effect in polycrystalline FCC metals, Acta Materialia 50 (14) (2002) 3641–3650.

[65] Y. Wei, X. Wang, M. Zhao, Size effect measurement and characterization in nanoindentation test, Journal of Materials Research 19 (1) (2004) 208–217.

[66] H. Li, A. Ghosh, Y. Han, R. Bradt, The frictional component of the indentation size effect in low load microhardness testing, Journal of Materials Research(USA) 8 (5) (1993) 1028–1032.

[67] J. Grunlan, X. Xia, D. Rowenhorst, W. Gerberich, Preparation and evaluation of tungsten tips relative to diamond for nanoindentation of soft materials, Review of Scientific Instruments 72 (2001) 2804.

[68] W. Nix, H. Gao, Indentation size effects in crystalline materials: a law for strain gradient plasticity, Journal of the Mechanics and Physics of Solids 46 (3) (1998) 411–425.

[69] Iso 14577-1:2002 metallic materials – instrumented indentation test for hardness and materials parameters – part 1: Test method, Iso 14577-1:2002 (2002).

[70] W. Findley, J. Lai, K. Onaran, Creep and relaxation of nonlinear viscoelastic materials: with an introduction to linear viscoelasticity, Courier Dover Publications, 1989.

[71] A. Fischer-Cripps, A simple phenomenological approach to nanoindentation creep, Materials Science & Engineering A 385 (1-2) (2004) 74–82.

[72] E. Lee, J. Radok, The contact problem for viscoelastic bodies, J. Appl. Mech 27 (3) (1960) 438–444.